Drag Reduction on a Flat Plate by Trapping Bubbles on the Surface

by

Kevin C. Marr

Thesis

Presented to the Faculty of the Graduate School

of The University of Texas at Austin

in Partial Fulfillment

of the Requirements

for the Degree of

MASTER OF SCIENCE IN ENGINEERING

The University of Texas at Austin

August 2005

Drag Reduction on a Flat Plate by Trapping Bubbles on the Surface

Approved by

Supervising Committee:

Acknowledgments

I would like to thank my supervisor, Dr. David Goldstein, for his support and guidance throughout the course of my undergraduate and graduate studies. I would also like to thank my partner, Mr. Romil Doctor, for his cooperation throughout this project.

Kevin Marr

The University of Texas at Austin

August 2005

Drag Reduction on a Flat Plate by Trapping Bubbles on the Surface

Kevin C. Marr, M.S.E.

The University of Texas at Austin, 2005

Supervisor: David B. Goldstein

The primary objective was to study the drag reduction on a flat plate with a dense distribution of trapped bubbles on the surface. A force balance and test apparatus was developed to measure the drag on a plate with and without bubbles. Bubble growth in cavities on the surface was observed and drag reduction was determined from the force balance and from wake surveys. Second, issues of manufacturing the plate surface were also considered.

The conclusions are that the trapped bubble drag reduction method shows promise in reducing drag. On one side of the plate, a dense group of bubbles covering about one-third of the surface was located near the leading edge of the plate. The bubbles covered about 7% of the total surface area of both sides of the

plate. It was found that the drag on a plate with bubbles produced a drag reduction compared to the plate with no bubble coverage for several of the test cases. At a Reynolds number of 2.09×10^5, a 5% drag reduction was measured by the force balance and wake survey. The largest drag reduction measured by the force balance was about 10% at a Reynolds number of 1.37×10^5. However, as the Reynolds number increased, the drag reduction generally decreased. At Reynolds numbers of 2.74×10^5 and 3.40×10^5, one of the test runs even showed a drag increase. A clear slip-like condition was not observed from velocity profiles of the boundary layer.

Contents

List of Tables

List of Figures

Chapter 1

Introduction

1.1 Motivation

Driven by recent increases in fuel costs, energy efficient technology has become a multi-billion dollar industry. Efficiency is often dependent on the energy required to overcome viscous drag. According to D.M. Bushnell, the annual economic loss due to drag is in the tens of billions of dollars (1997).

For submerged vessels and pipelines, liquid flow over a solid surface causes hydrodynamic drag due to shear stresses that arise from the no slip condition: the velocity of the liquid at the surface must be the same as the velocity of the surface. However, not all interfaces have a no-slip condition. For a liquid-gas interface, such as an air bubble in water, the interface experiences near free motion with the liquid. Of course, there still exists no slip between the liquid and

the gas, but the shear stress in the liquid on such an interface may be effectively reduced because the velocity gradient at the interface is small. If a hull of a ship or wall of a pipe could be made with a slip surface, the drag reduction associated with the slip surface could effectively reduce the power required to propel a ship or pump fluid through a pipeline. Although it is not possible to coat an entire hull of a ship with a liquid-gas interface, it may be feasible to trap thousands of small air bubbles on the hull. As liquid flows over the bubble surface, the bubble surface moves with the liquid, thus reducing the net viscous drag over the hull.

This study presents a method to trap air bubbles in small cavities on the surface. The bubbles are produced by electrolyzing the water in the cavities, and they are held in place by interfacial tension. It is hypothesized that the turbulent boundary layer over the surface experiences reduced shear flow over the bubble surfaces and the overall viscous drag is reduced.

1.2 Objectives

Drag reduction due to trapped air bubbles in water is based on the observation that the bubble interface moves freely with the flow resulting in an induced slip-like condition on the bubble surface. Trapped air bubbles may prove to be more effective than surface textures such as riblets, require less energy than microbubble injection, and have no environmental concerns or containment requirements of dilute polymer injection. However, the trapped air bubble

concept has yet to be proven in practice. Therefore, the scope of this thesis is an experimental proof of concept.

Experiments are conducted on an acrylic flat plate mounted on a force balance in a water channel. The drag on the plate can be determined by direct measurement by the force balance and via momentum balance computations on velocity profiles taken by a Laser Doppler Anemometer. The primary objective is to determine whether there is drag reduction due to trapped bubbles on the flat plate. The flat plate can be configured as a simple solid flat plate or a bubble plate. The bubble plate configuration has thousands of bubbles trapped in small non-thru holes drilled in to one side of the plate. The drag on the two configurations is then compared to determine if there is a drag reduction caused by the trapped bubbles.

A secondary objective of the project is to address some feasibility issues. First, in order to produce the bubbles by electrolysis, the internal cavity surface must be conductive while the plate surface is non-conductive. Various designs and the associated manufacturing issues are investigated.

1.3 Thesis Overview

A review of previous work in the field of viscous drag reduction is presented in Chapter 2. These works include microbubble injection, chemical

additives, and surface textures such as riblets and nanostructure skins. Work in bubble growth and bubble detachment from cavities is discussed as well.

Chapter 3 details the experimental program. It includes descriptions of the flow facility, measurement systems and capabilities, the experimental apparatus, and the flow conditions.

Chapter 4 begins with a summary of the bubble production observations and concludes with drag and velocity profile comparisons between a flat plate surface, a drilled plate surface with bubbles, and a drilled plate surface without bubbles.

Concluding remarks and future work plans are discussed in Chapter 5.

Chapter 2

Literature Review

2.1 Microbubble Injection

Microbubble drag reduction is commonly achieved by injecting a cloud of microbubbles into the turbulent boundary layer by either bubble generation via electrolysis or direct injection through slots or porous skins. The first of such attempt was reported in 1973 by McCormick and Bhattacharyya. They generated hydrogen bubbles by wrapping a copper wire around a towed body and dissociating the surround water and showed that the drag on the towed body was reduced. However, they were unable to determine the detailed mechanisms of the drag reduction because of the pressure gradients and boundary layer transition on the towed body. A few years later, a group of Soviet scientists employed an injection technique by forcing air through a 1-50 μm sized pores on a flat plate

and measured local skin friction, bubble concentrations and velocity profiles (Migirenko and Evseev 1974). They reported a local skin friction reduction of nearly 10% near the porous section; however, further downstream, they noticed that the boundary layer gradually relaxes back to an undisturbed profile.

Further experimental work has expanded the understanding of microbubble injection. Madavan *et al* (1984, 1985a,b) found skin friction reductions, as high as 80% in a microbubble injected liquid turbulent boundary layer, depending on the injection flow rate. They also hypothesized that microbubbles reduce drag by decreasing the viscosity near the buffer region and retarding turbulent production near the wall. Pal *et al* (1988) determined the drag reduction was effective as long as the microbubbles were located in the buffer region.

More recent studies have focused on microbubble injection applications for ship hulls. One of the more important issues is the scale effect for large ships. Watanabe *et al* (1998) measured local skin friction reduction due to microbubble injection on 20 m and 40 m long flat plates in a towing tank facility. The microbubbles were injected 1.2 m from the leading edge at various gas flow rates. They found that the local skin friction reduction was greater at larger gas flow rates, and the largest local skin friction reduction was about 50%. Kodama *et al* (2000) furthered the study of microbubble drag reduction in a circulating water

tunnel specifically designed for microbubble experiments. Their skin friction results agreed with Watanabe's findings even though their test apparatus was much smaller than Watanabe's flat plate. They also expanded the scope of their experiment by comparing drag reductions from bubble injections through a porous skin surface and a perforated surface at three different tunnel speeds. Both surface types produced similar skin friction reduction. However, for ship applications, net drag reduction (energy saved from the drag reduction minus the energy required to produce the bubbles) must be achieved. Both studies say that the proper scaling parameter for net drag reduction should not be the boundary layer thickness, but neither was able to determine the proper scaling parameter to predict net drag reduction for a ship.

Microbubble injection is different than the proposed trapped bubble method. Microbubble injection techniques inject bubbles at high injection gas rates into the buffer region of a liquid boundary layer. It has been suggested that microbubble injection reduces drag by reducing the viscosity near the buffer region and retarding the turbulent production near the wall. The trapped bubble method produces bubbles in holes on the surface at a low gas production rate via electrolysis of the water, so that the bubbles do not detach from the holes. Although the drag reduction method for trapped bubbles has not been studied

previously, the proposed method is based on the observation of an induced slip condition on the bubbles surface.

2.2 Chemical Additives

Another method of drag reduction is to add high molecular weight polymers to the liquid boundary layer flow. First discovered in 1948 by Toms, chemical additives have shown much promise over the past half-century. With the addition of a few tens of parts per million by weight of long-chain polymers, drag reduction in channels and pipes can be as high as 80%. To date, many polymers and solvents have shown significant drag reduction. One of the most common polymer-solvent combinations is polyethylene oxide (PEO) in water due to its low cost and effectiveness. Virk *et al* (1967) found adding 18 ppm PEO in a water boundary layer resulted in a 33% skin friction reduction compared to water alone. Hoyt (1972) concluded that polymers with long linear structures with few or no side chains were the most effective.

Although there has been extensive experimental work in dilute polymer drag reduction, the reduction mechanism is unclear. One of the leading explanations is that the viscoelastic properties of the polymers inhibit near wall turbulent fluctuations and therefore reduce local turbulence production (Tiederman *et al* 1985). Recently, near-wall particle image velocimetry (PIV) measurements have the compared the near-wall turbulent structure in a polymer

drag-reduced flow to its Newtonian counterpart (White *et al* 2004). As the drag reduction increased, the spanwise separation of the low-speed velocity streaks increased, and the strength and number of near-wall vortices decreased. In a numerical study, Yarin (1997) further detailed this near-wall mechanism. His simulations showed that for a turbulent boundary layer without additives, interaction between spanwise vortex perturbations and background shear flow led to strong vortex stretching and the emergence of horseshoe-like vorticies. However, the presence of dilute polymers suppressed the stretching of these spanwise vortices resulting in a more gentle mean velocity profile.

None of the mentioned studies address the applicability of chemical additives to ship drag reduction. The studies do not compare the power required to inject the polymers or energy cost required to carry the polymers with energy savings from the drag reduction. Also, environmental issues are not discussed.

Chemical additives are more similar to microbubble injection than the trapped bubble method in that external matter is injected into the boundary layer. Similar to microbubble injection, chemical additives are proposed to reduce drag by suppressing near-wall turbulent production mechanisms. Unlike trapped bubbles, the chemicals are not specifically designed to affect the boundary condition of the surface.

2.3 Passive Surface Textures

Passive surface textures include riblets and nanostructure skins. Streamwise aligned micro-scaled grooves, or riblets, have been experimentally shown to reduce drag on a surface about 5-10%. In an effort to optimize riblet shapes, Walsh (1980, 1982, 1983) conducted a series of studies finding that a symmetrical V-shaped riblet surface results in a maximum drag reduction of 8%. Pollard (1997) hypothesized that riblet drag reduction is limited to 10% because its interaction with quasi-streamwise vortices is inefficient: the riblets only displace structures away from the wall and do not significantly suppress the turbulent production mechanism.

Nanostructure skins and compliant coatings have also shown a reduction of skin friction on the 10-20% level. Balasubramian *et al* (2003) is studying nanostructure skins that emulate the bumpy surface microstructure of lotus leaves and renders the skin hydrophobic. He proposed that a droplet does not wet the surface, air is trapped between the bumps on the surface, and drag is reduced because of the lower dynamic viscosity of the air layer. The nanostructure skins have shown drag reductions of 15% on pipes and 20% on a flat plate. However, the effect of the coating diminished over time. Also, Balasubramian does not consider turbulent boundary layers in his investigation.

Choi (2000) summarizes the results of drag reduction due to compliant coatings in a review of the work conducted at the University of Nottingham. Compliant coatings are flexible coatings inspired by dolphin skins. Choi's results show a 7% drag reduction over a range of test speeds for a wall-bounded flow. In theory, the compliant coatings should delay the transition from laminar to turbulent boundary layers (Lucey and Carpenter 1992).

Passive surface textures are similar to trapped bubbles because both are intended to manipulate the surface. But, it has been suggested that riblets, like microbubble injection and chemical additives, reduces drag by affecting the turbulent production, and compliant coatings theoretically delays laminar to turbulent transition. Nanostructure skins are perhaps the most similar to trapped bubbles. Both methods trap air on the surface in an attempt to reduce the shear rate over the surface; however, the air layer trapped on the nanostructure skin is not intended to provide a slip-like surface, but to de-wet the surface. Moreover, there is no obvious mechanism to replace the air lost over time.

2.4 Trapped Bubble Drag Reduction

The bubble drag reduction method presented here is quite different than microbubble injection and chemical additives, but related to nanostructure skins and compliant coatings. The trapped bubble method assumes that the bubble interface moves with the flow and induces a slip-like condition on the bubble

interface. Because the bubble interface moves with the flow, the shear stress on the bubble's surface is smaller than that of a solid surface. By trapping bubbles, the bubble surface effectively replaces solid surface, and therefore, the net shear stress on the entire surface should be reduced.

2.4.1 Slip Condition

The bubble surface can be assumed to be a slip-like surface because the interface moves with the liquid. However, as surfactant builds up on the interface, particles can cause portions of the interface to revert back to a no-slip boundary condition—the near-surface flow over the particles stuck on the surface bay have zero velocity. Matsumoto and Matsurra (2004) studied surfactant build up on a bubble using a large-scale molecular dynamics (MD) simulation. They simulated bubbles rising in a liquid and showed that flow around a bubble has a finite velocity on the bubble surface and that the terminal velocity of the bubble agreed well with theoretical predictions. They observed that as surfactant absorbed on the bubble surface built up at the rear end of the bubble, the velocity with respect to the bubble center of the bubble surface went to zero and the terminal velocity of the bubble decreased.

Trapped bubble drag reduction is based on the slip-like condition on the bubble surface. If contamination causes the bubble surface to revert to a no-slip condition, the effectiveness of the bubbles may be compromised. For proposed

applications on ship hulls and pipelines, the fluid may have high concentrations of contaminants. If the shear on the bubble surface is insufficient to purge or displace the surfactants, a method to clean the bubble surface may be required. Instead of physically cleaning the surface, it may be possible to periodically purge the bubbles from the cavities and regenerate the bubbles.

2.4.2 Electrolysis

The proposed technique, detailed in Chapter 3, calls for the bubbles to be produced via electrolysis. According to Faraday's Law of Electrolysis, the mass flow rate of the produced hydrogen, $\dot{m}_H$, is

$$\dot{m}_H = \left(\frac{IM}{zF}\right) \qquad \text{(Eq 2.4.1)}$$

where I is the electric current, M is the molecular weight of hydrogen, and z is the valence number. Faraday's constant, F, is 9.65×10^7 Coulombs/kmol. For the experimental bubble plate, the current applied to the plate is very small, approximately 0.1 to 0.3 amperes. Therefore, the production rate of the hydrogen is very small, about 2×10^{-9} to 6×10^{-9} kg/s.

2.4.3 Bubble Growth Historical Review

The bubbles in the cavities need to be produced and remain stable in static and liquid cross flow conditions. Therefore, the dynamics of bubble growth and detachment is briefly considered and related works are discussed.

Much of the current research in bubble formation and growth is rooted in work done in the 1950s and 60s. The following summary of bubble research is taken primarily from Kumar and Kuloor's chapter, *Formation of Bubbles and Drops*, in Advances in Chemical Engineering (1970).

In Figure 2.4.1, gas is injected through an orifice into a fluid. As a result, a bubble forms at the opening and grows.

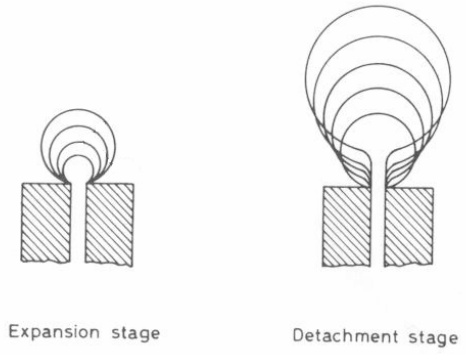

Figure 2.4.1: Schematic of Gas Injection into a Fluid (taken from Kumar and Kuloor 1970)

The bubble grows until it reaches a critical size and then detaches from the orifice. In its simplest form, bubble growth and detachment from an orifice or

cavity in a horizontally oriented surface can assumed to depend on three main forces. In a quiescent fluid, buoyancy due to pressure differences across the liquid-vapor interface acts upward, while gravity and capillary forces due to the interfacial tension act downward. In general as bubbles increase in size, the buoyancy force increases and the bubble surface tension decreases. By balancing the forces, the maximum size of the bubble before it breaks away from the cavity can be determined.

Many parameters influence the maximum size a bubble can achieve before detachment. However, in the present study, the liquid and gas are predetermined, and therefore, only the effects of cavity shape and low gas flow rates are considered. Studies found that at low gas flow rates, the maximum bubbles volume is directly proportional to the orifice diameter. In addition to orifice diameter, orifice geometry also plays a role in bubble growth. In 1964, Krishnamurthi, Kumar, and Datta compared different hole shapes such as triangles, squares, etc. to circular holes. At low injection flow rates, they found that for equal-area geometries, the maximum bubble volume is similar but not exactly equal. Varying the size of the cavity should be more effective in controlling the maximum bubble size than changing the shape of the cavity.

2.4.4 Kumar and Kuloor Bubble Model

Kumar and Kuloor (1970) proposed the following model for bubble growth and detachment from a horizontally oriented orifice for a single bubble in a static fluid. The model is based on two stages of bubble expansion. The first expansion stage ends when the buoyancy, gravity, and surface tension forces acting on the bubble are in equilibrium. The second stage ends when the bubble detaches. For an inviscid liquid with surface tension, the second-order approximation of the final bubble volume, V_F, can be simplified to

$$V_F = \frac{\pi d_C \gamma \cos\theta}{(\rho_l - \rho_g) g} \qquad \text{(Eq 2.4.2)}$$

where d_c is diameter of the cavity, γ is the surface tension between the gas in the bubble and the surrounding liquid, θ is the contact angle of the bubble interface with respect to the solid surface, ρ_g and ρ_l are the densities of the gas and liquid, and g is the acceleration due to gravity. The full model is presented in Appendix A.1. Kumar and Kuloor also extended their bubble model to account for orifice orientations for non-horizontal surfaces (Appendix A.1).

2.4.5 Bubble Growth with Cross-Flow

Much of the work discussed thus far has been for bubbles with no liquid flow. More current studies have investigated the effects of a cross-flow on bubble dynamics. Marshall *et al* (1993) developed a system of first-order equations to

model spherical bubble growth in a constant velocity cross flow. Figure 2.4.2 shows a diagram of the physical system.

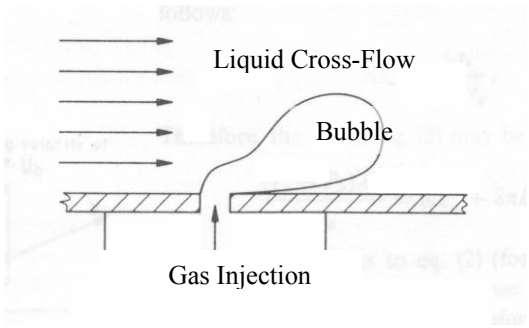

Figure 2.4.2: Schematic Bubble Growth in a Cross-Flow (taken from Marshall 1993)

The model is derived from the equation of motion for the bubble expansion, the equation of motion for the bubble translation, the gas flow, and the pressure distribution around the bubble. The resulting second-order system is then reduced to a first order system with six unknowns and six equations. To validate the model, Marshall *et al* compared predicted bubble departure size with experimental results for various orifice diameters, gas flow rates and cross flow velocities. Overall, their predicted values were within 25% of the experimental results.

More recently, Nahra and Kamotani (2003) developed a force balance-based bubble detachment model for the same physical system. Although their model was developed for low gravity conditions, they were able to apply the

model to normal gravity conditions by changing the gravity level and detachment criterion. They compared their model to a modified Kumar-Kuloor approach. To account for a cross flow in the Kumar-Kuloor model, Nahra and Kamotani expanded the model to two dimensions by simultaneously solving the equations of motion for both horizontal and vertical translations and the expanding bubble. Nahra and Kamotani found both models had good agreement with normal gravity experiments.

However, these studies only account for a single isolated bubble. In the trapped bubble method thousands of bubbles are produced in cavities on the surface. Furthermore, the bubbles on the surface are in close proximity of each other. Therefore, these force balance methods for a single bubble may not apply to groups of bubbles.

Chapter 3

Experimental Program

3.1 Water Tunnel

The experiments were conducted in an Eidetics model 1520 closed-loop water channel located in of the W. R. Woolrich Laboratories at the Universtiy of Texas, Austin. Water is pumped up through a 12-inch diameter PVC pipe into a large settling chamber, and then passed through a series of mesh honeycomb screens before accelerating through a 6:1 ratio contracting nozzle into the test section. The water is then diverted down through PVC pipes and returned to the reservoir. The channel test section is 64 inches long and diverges slightly downstream to accommodate the growing boundary layer on the channel walls. The upstream test cross-section is 15 by 20 inches, and the downstream cross-section is 15.25 by 20 inches. Clear glass walls run the entire length of the test

section and allow visual access to the channel from the sides and below. The top of the channel is left open to allow mounting access for test models. Another window, perpendicular to the flow direction, is located at the end of the tunnel where the water is diverted and allows for visual access behind the test model.

The tunnel free stream is adjusted by increasing the rotation speed of the 2-Hp electric motor that drives a 900 gpm capacity Cascade Model 8P axial-flow pump. The control panel has an analog indicator for the pump RPM and a digital indicator for the flow rate. The water tunnel has a maximum free stream of 1 ft/s and an advertised turbulence intensity level of less than 1.0% RMS.

The tunnel also has flow visualization capabilities. Water-based dye can be injected into the test section from six dye canisters.

3.2 Laser Doppler Anemometer

Streamwise flow velocity measurements are taken with a Dantec Dynamics, Inc. BSA F50 single component Laser Doppler Anemometer. The LDA system consists of three components—a two-dimensional traverse, a FlowLite 2D, and a BSA F50 Flow Processor. The traverse has a 0.01 mm resolution in two orthogonal directions over a 1 m range and is controlled by a C116-4 Schrittmotor-Controller. The FlowLite houses a Class C 632.8 nm laser and a photomultiplier tube (PMT). The beam is sent to a laser probe mounted on the traverse via a fiber optic cable, and the PMT detects the phase shift and sends

the signal to the processor. The processor interfaces both the FlowLite and the traverse system with a Pentium III PC through BSA flow software.

3.3 Force Balance

A force balance is positioned above the open top section of the water channel and clamped to the horizontal support beams (Figure 3.3.1).

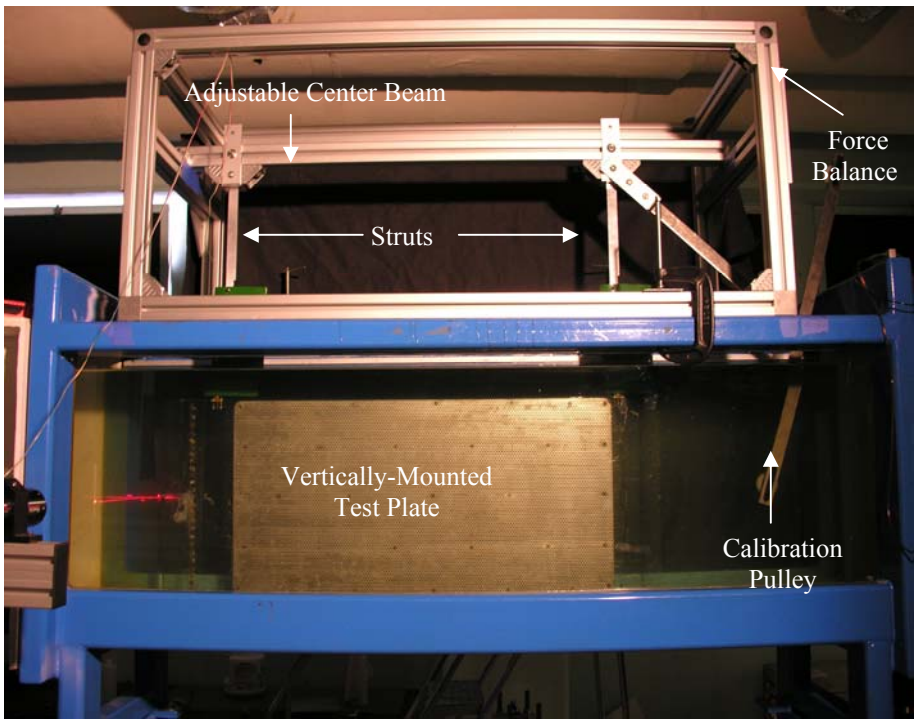

Figure 3.3.1: Force Balance

The test plate is hung vertically by two mounting structures each consisting of a flexure and a strut. The struts are attached to an adjustable center beam, and the flexures are attached to the strut. The plate is then attached to the flexures with a

pair of right-angle brackets. Drag is obtained by measuring the strain on the flexure attached to the leading strut. The leading flexure has four strain gages mounted in pairs on each side. The gages are oriented so that the front pair measures extension and the aft pair measures compression. Each flexure is optimized for up to a Newton of force. A NACA 0012 airfoil fairing is mounted on each strut surrounding the entire mounting structure. The fairings extend into the water channel shielding the flexure from the flow.

By using multiple strain gages in a Wheatstone bridge circuit, the compression and extension on both sides of the flexure are measured. This allows the internal strain of the force balance structure to be zeroed and amplifies the output signal. As the plate is displaced, the strain signal is sent to a Pentium III PC via a National Instruments BNC-2120 connector board and a PCI 6013 data acquisition (DAQ) card. A National Instruments Labview Virtual Instrument (VI) software interface allows the user to define the sampling rate and the total number of samples.

The signal is related to drag by a simple calibration technique. A calibration factor is found by loading the plate with known values and measuring the resultant strain voltage. The calibration structure consists of a two-pulley system attached to the center beam near the downstream strut. A fiber is hooked to the back of the plate and fed through the pulleys. As weights are loaded at the

other end of the string, the plate is displaced and a voltage signal is measured. The calibration factor is found from the slope of the linear curve fit of the plot of weight vs. voltage. Figure 3.3.2 shows a typical calibration curve taken with five weights.

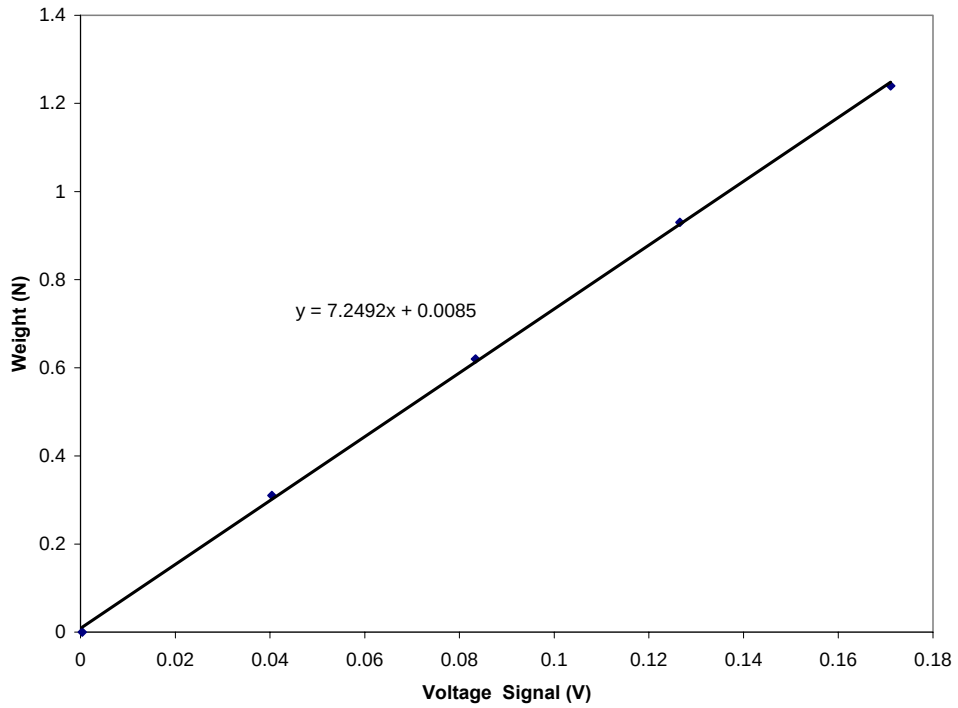

Figure 3.3.2: Typical Force Balance Calibration Curve

The calibration constant is the slope of the trendline. The force balance is calibrated for the test plate with no flow in the channel before each test run. Calibration is required whenever the internal stresses of the force balance are

changed by adjusting the angle of attack of the center beam, removing and remounting the plate, or adjusting the plate to be vertical.

3.4 Flat Plate

The test plate is made up of an acrylic mounting plate and thin metal insert plates. The metal insert plates are mounted into a cavity one side of the acrylic plate. Bubbles are to be trapped in non-thru holes drilled into the metal plates. The advantage is that multiple hole configurations can be tested without having to machine multiple acrylic plates. Also, the metal plates provide the conductivity required for electrolysis.

3.4.1 Acrylic Mounting Plate

The acrylic mounting plate and measures 30.75 by 15 by 0.75 inches. It has a 4:1 ratio elliptical leading edge and a 20° tapered trailing edge (Figure 3.4.1).

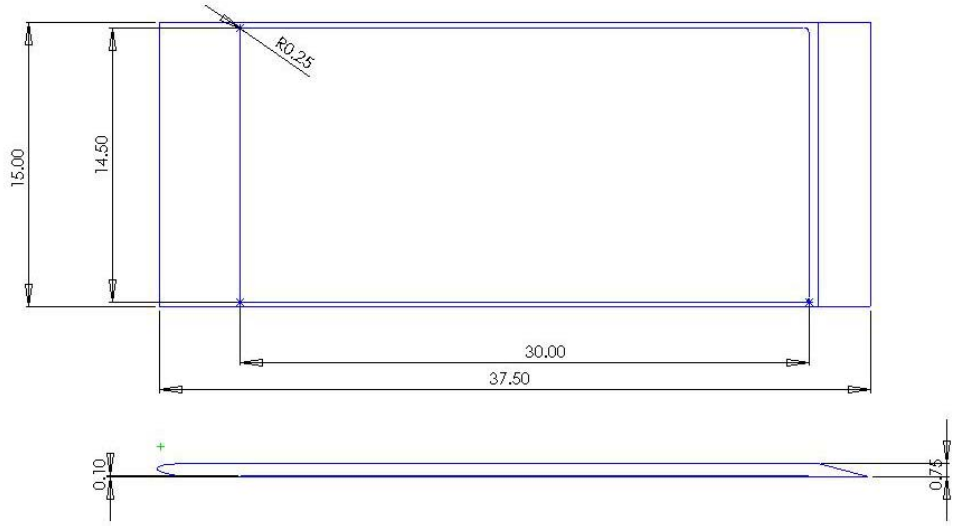

Scale in Inches

Figure 3.4.1: Schematic of the Acrylic Test Plate

The trailing edge is only half tapered where one side of the plate inclines 20° and the other side of the plate remains flat. The flow over the completely flat side of the plate is forced to separate at the trailing edge regardless of tunnel speed and nature of bubble effects, whereas, the flow over the tapered side of the plate may separate at different locations depending on the tunnel speed. Therefore, if the bubbles are produced on the completely flat side of the acrylic plate, the flow on the flat side of the plate should separate at the trailing edge regardless of bubble influences. Two and a half inches from the leading edge, 25 half-inch hexagonal nuts serve as boundary layer trips on each side of the plate. On the flat, non-

tapered side of the acrylic plate behind the boundary trips, a 30 by 14.5 by 0.1-inch cavity with 0.5 inch rounded corners is routed to accommodate different bubble plate configurations. The plate is generally mounted vertically in the test channel and is attached to each force balance flexure by two right angle brackets. The mounting area is notched 0.25 inches to accommodate the bracket thickness. On the tapered side of the plate, a 0.05 inch circular hook mount is attached 1.25 inches from the trailing edge along the centerline of the plate. The hook mount allows for the calibration system to easily attach to and detach from the plate.

3.4.2 Aluminum Bubble Plates

Three interlocking 0.0625-inch thick metal plate inserts are mounted in the acrylic plate cavity by counter-sunk flat-head screws (Figure 3.4.2).

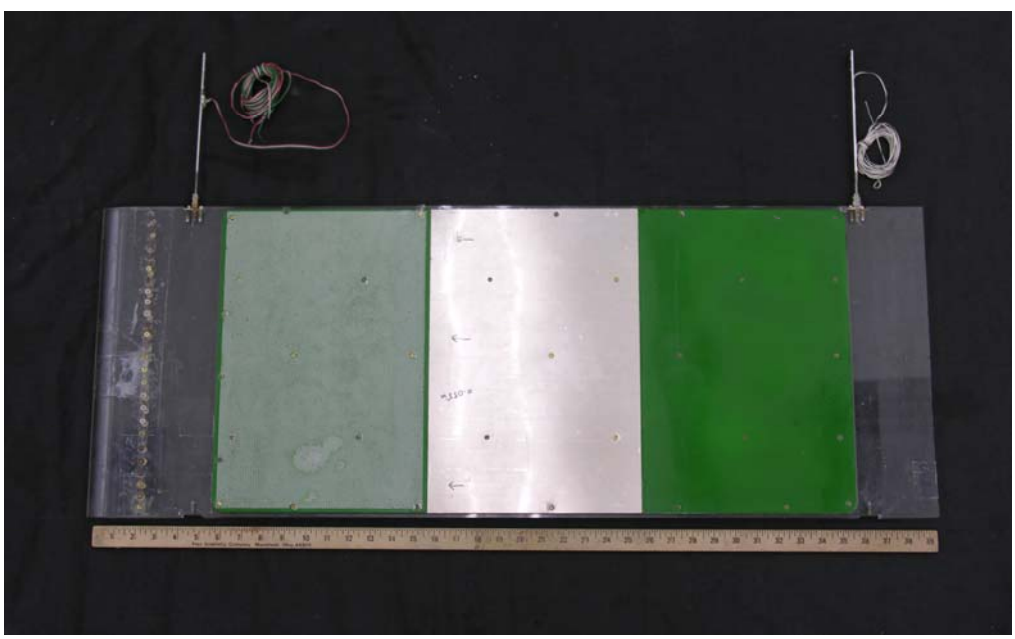

Figure 3.4.2: Aluminum Plates Mounted in the Acrylic Plate Cavity

A tenth-inch piece of black foam is placed in between the metal plate and the acrylic plate. As the metal plate is screwed in to the mounting cavity, the foam compresses allowing the plate to be leveled. The forward and aft plates are identical and are 10 by 14.5 inches. One 14.5-inch side has half-inch rounded corners that match the acrylic cavity; the other 14.5-inch side has a 45° chamfer (Figure 3.4.3).

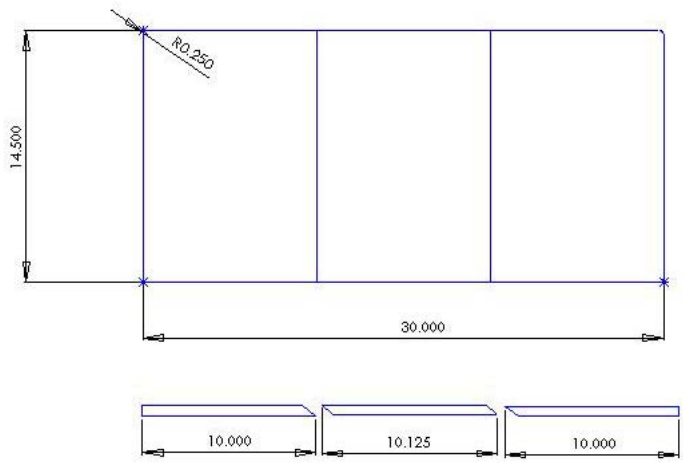

Scale in Inches

Figure 3.4.3: Schematic of the Aluminum Plates. (*Thickness of the aluminum plates are exaggerated to show the chamfer)*

The middle plate is 10.125 by 14.5 inches and has 45° chamfers on both 14.5-inch sides. The chamfered sides insure that the plates are level when screw mounting.

The metal plates are machined from 6061 aluminum and airbrushed with a waterproof POR-15® Hardnose two-component coating. This coating is similar to boat paints and hardens as it cures. The coating consists of one part hardener to four parts color coat; xylene is added to thin the paint for airbrush application. Prior to airbrushing, the aluminum plates are polished and prepared with a self-etching solution and metal primer. First, POR-15® Metal-Ready etching solution is applied. The solution etches the aluminum and leaves a zinc phosphate coating to enhance adhesion. Then, a single coat of Tamiya Metal Primer is sprayed on to the aluminum before applying the final paint coating. Because the subsequent hole drilling process tends to pull up the paint as the drill bit exits the hole, the two preparation steps are necessary to provide adequate adhesion.

Small non-thru holes are drilled by a programmable CNC machine into the painted aluminum plates (Figure 3.4.4). The drilling process exposes the bare aluminum so that the flat surface is covered by paint and the holes are not. In this first round of testing, only the forward plate has holes drilled. The cavities are 0.046-inch diameter holes drilled 0.03 inches into the aluminum plate in a staggered pattern (Figure 3.4.5).

Figure 3.4.4: Drilling of the Forward-Most Aluminum Plate

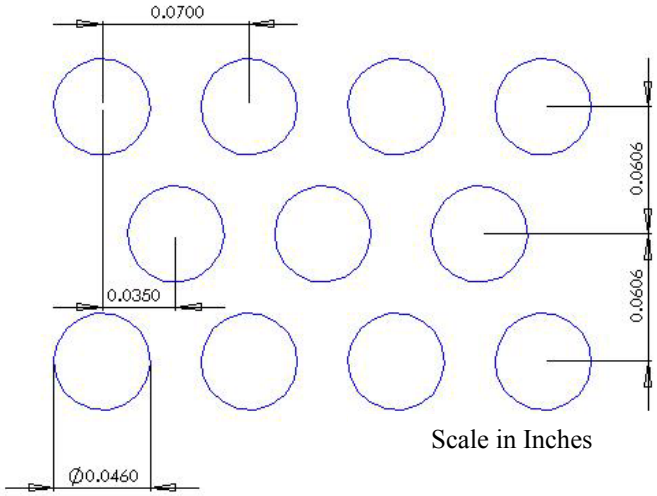

Figure 3.4.5: Hole Pattern

The staggered pattern increases the hole coverage compared to a square grid pattern. The staggered pattern is achieved by offsetting alternate rows. The holes in each row are spaced 0.07 inches apart from center to center; each row is spaced 0.0606 inches apart from center to center. The non-offset rows consist of 205 holes. The offset rows consist of 204 and are offset 0.0035 inches. The entire hole pattern consists of 160 total rows. The holes cover approximately 37.5% of the forward bubble plate.

Although the forward plate was treated with self-etching solution and metal primer, about 2 in^2 of the coating pulled off in during the drilling process. These areas were airbrushed again without masking the holes. The paint-filled holes were then cleared by a manually re-drilling the hole with a power drill.

3.4.3 Electrolysis and Corrosion Issues

The painting and drilling process results in a non-conductive surface and conductive holes. By applying a weak current through the plates, bubbles form in the exposed holes via electrolysis of the water. Figure 3.4.6 shows a diagram of the electrolytic circuit.

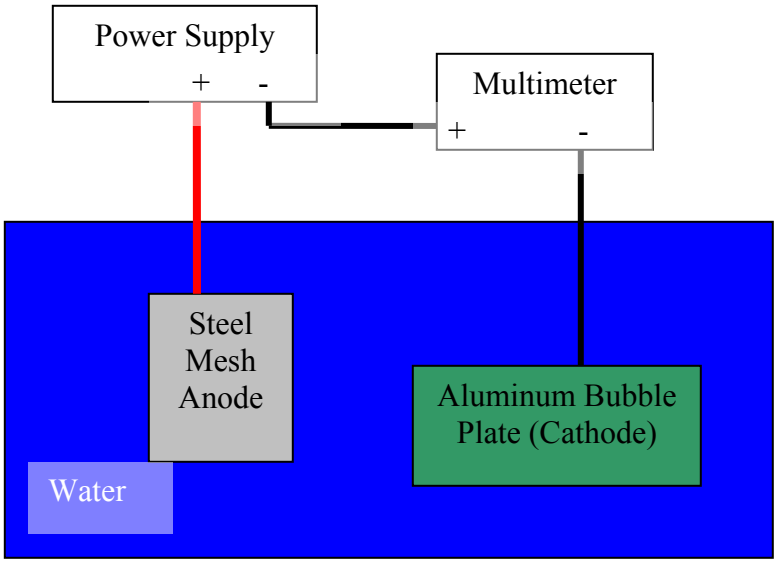

Figure 3.4.6: Electrolytic Circuit of the Plate and Mesh Anode

The electric current is provided by a variable 20 volt Micronta Adjustable Dual-Tracking DC Power Supply. The bubble plate is attached to the negative pole through a wire wrapped around one of the mounting screws; the plate thus becomes the cathode. A single bare countersunk hole provides a contact point for the metal screw. The countersunk contact point is painted with M.G.Chemicals® Nickel Print. The nickel paint enhances conductivity and reduces the galvanic corrosion between the metal screw-aluminum plate interface (Davis 1999). A stainless steel mesh sheet is attached to the positive pole and placed in the water to become the anode. The orientation of the electrolytic circuit is dictated by

corrosion. The bubble plate is chosen to be the cathode so that hydrogen is produced on the bubble plate and oxygen is produced on the steel mesh. The steel mesh is less prone to oxidation than aluminum. If the two leads were to be switched, oxygen would be produced on the aluminum. A layer of aluminum oxide would grow on the aluminum producing a thick powdery layer.

In addition to the nickel paint and cathode selection, other precautions are taken to reduce corrosion during testing. The water in the channel is not treated with chlorine or bromine, and thus the corrosive environment in the test section is reduced. Also, stainless steel mounting screws are used to prevent rust. In theory, only 1.3 volts are required to dissociate water. However, for the current test setup, the steel mesh is placed about 7 inches away from the bubble plate. Because the current is a function of the distance between the cathode and anode, a higher voltage, at least 10-15 volts, is required to draw enough current to dissociate the water at reasonable production rates. In general, the voltage is turned off during testing due to voltage interference with the force acquisition system.

3.4.4 Other Manufacturing Considerations

Other methods of manufacturing a bubble plate with a non-conductive surface and conductive holes were also considered. One of the more straightforward designs was to paint off-the-shelf perforated metal plates.

However, the paint tended to fill the holes. Because of the small hole size and number of holes, it was not feasible to manually clean all the holes. Masking techniques were tried, but unsuccessful. To mask the holes from the paint, silicon-based caulking and clay were used to fill each hole, but the cured silicon could not be removed easily from the holes and small bits of clay stuck in the holes could not be blown out by pressurized air. Perforated plates also proved to be susceptible to air leaking from the bubbles through the gap between the foam backing and the perforated plate. Laser drilling would have saved considerable drilling time, but the laser drilling companies surveyed said their process only produces thru holes and aluminum is too reflective to be effectively laser drilled.

Instead of painting, anodizing the aluminum was also considered. The anodizing process provided a drillable hard, smooth non-conductive surface, but electrolysis testing resulted in severe pitting of the anodized surface. On sample test plates, the anodized aluminum began to pit after applying 9 volts for approximately three hours. A more exotic manufacturing method investigated was etching conductive holes with the offset printing technique used for newspaper printing. However, the etching did not produce enough relief in the plate to trap bubbles.

Aluminum was selected as the plate material because it is easily machined. However, aluminum is more vulnerable to corrosion than other metals. It is

possible, and perhaps better suited, to use other metals such as stainless steel. To ameliorate the aluminum corrosion problem, gold plating of the holes themselves was attempted. A few test samples were painted and drilled before undergoing the plating process. After the gold plating, however, the paint coating came off as the piece was being blown dry; both the holes and the flat surface were plated in gold. Further material studies are necessary to optimize the manufacturing process.

Chapter 4

Results

4.1 Observation of the Slip Condition and Effect of Surfactant

The trapped bubble method is based on the observation that a clean bubble surface moves with the flow and induces a slip-like boundary condition. However, it has been noted that contamination can cause the bubble surface to exhibit a no-slip-like condition. To investigate the bubble slip condition, the acrylic plate was mounted in the water channel without the aluminum plate inserts, and oriented so that the cavity faced downward, and a single large bubble was injected into the cavity filling the entire cavity area (Figure 4.1.1).

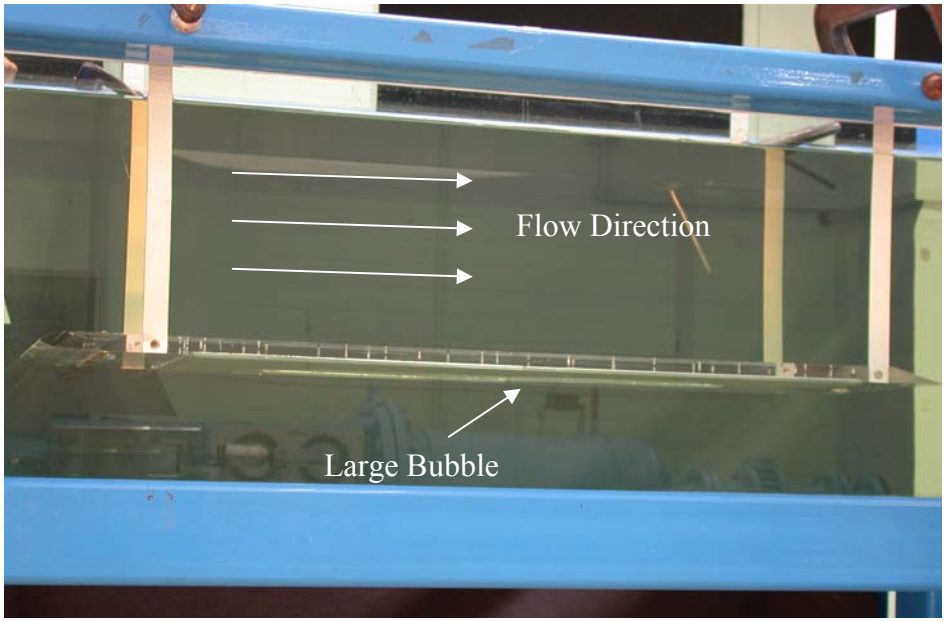

Figure 4.1.1: Acrylic Plate Mounted Horizontally

The upward buoyancy force allowed the bubble to stay in the cavity. The large bubble represents a more ideal case where the entire surface is made up of the bubble interface. Here, slip can be measured more easily with the LDA, and the interface can be more easily observed. With no freestream flow the bubble was horizontal and "mirror flat". As the freestream velocity was increased, a variety of phenomena were observed.

At a tunnel freestream of 0.13 m/s, it was observed that the bubble surface was not uniformly level—the bubble surface was slightly raised toward the back of the bubble forming a ridge-like structure across the width of the bubble surface (Figure 4.1.2)

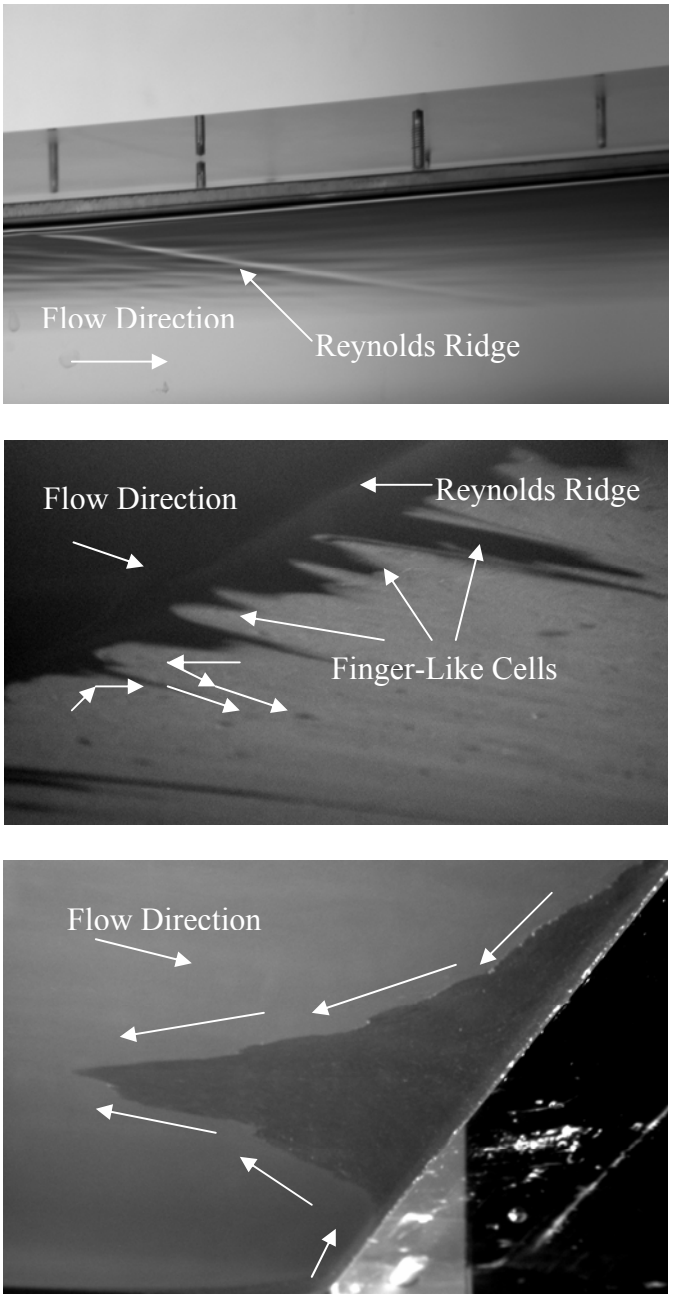

Figure 4.1.2: Reynolds Ridge. **The freestream velocity is 0.13 m/s.** ***Top:*** **Reynolds ridge is shown on the bubble surface beneath the acrylic plate. Upstream, to the left, of the ridge the surface is clean. Downstream, to the right of the ridge, the surface is contaminated.** ***Middle:*** **Finger-like circulation cells just downstream of the ridge.** ***Bottom:*** **Heart-shaped large circulation cells at the downstream edge of the bubble.**

This ridge, called a Reynolds ridge (Satterly and Turnbull 1929), delineates the clean bubble surface from the contaminated bubble surface. The visable particles adhering to the bubble surface behind the Reynolds ridge were not static. Surfactant particles moved along the bubble interface forming long, streamwise circulation cells. It was easy to observe both downstream and upstream motion of the particles that adhered to the surface. Just after the ridge, the circulation cells were long and skinny forming a finger-like pattern. At the downstream edge of the bubble, two large circulation regions formed a heart-shaped pattern that circulated particles from the outer edge of bubble to the centerline of the bubble. Smoke visualization of the flow inside the bubble showed that the air moved downstream and accumulated at the back of the bubble behind the Reynolds ridge. Also, the Reynolds ridge moved upstream as surfactant built up at the back of the bubble. After an eight hour period, the ridge had moved upstream several inches and a larger surface area of the bubble was contaminated. The ridge moved forward at a rate of about one inch every hour.

A slip-like condition was easily observed on the clean bubble surface upstream of the Reynolds ridge. However, even though adhering particle motion was observed in the fingers at the back of the bubble, a net no-slip condition was measured downstream of the ridge. Figures 4.1.3 compares the LDA measured boundary layer profiles on the bubble upstream and downstream of the Reynolds

Ridge. The velocity, U, is normalized by the freestream velocity, U_{inf}, and plotted with respect to the the similarity variable, $\eta = y\sqrt{\frac{U_{\inf}}{2\nu x}}$, where ν is the kinematic viscosity and x is the streamwise location from the leading edge of the plate. Figure 4.1.4 shows the streamwise RMS velocity, u_{rms}, plotted with respect to η.

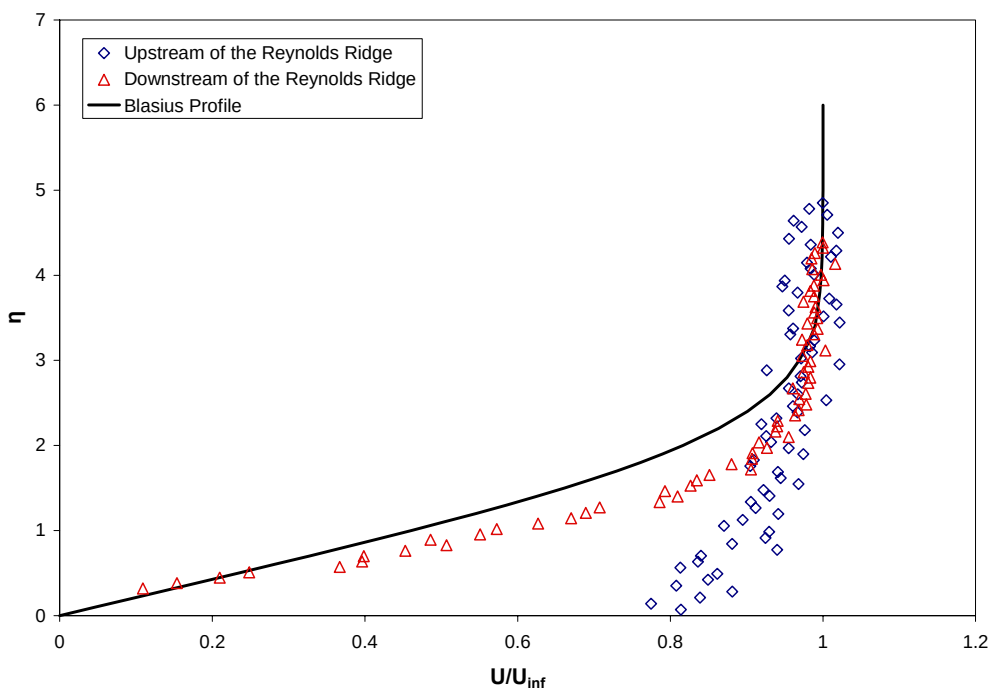

Figure 4.1.3: Boundary Layer Profiles Upstream and Downstream of the Reynolds Ridge at $Re_L = 1.2 \times 10^5$

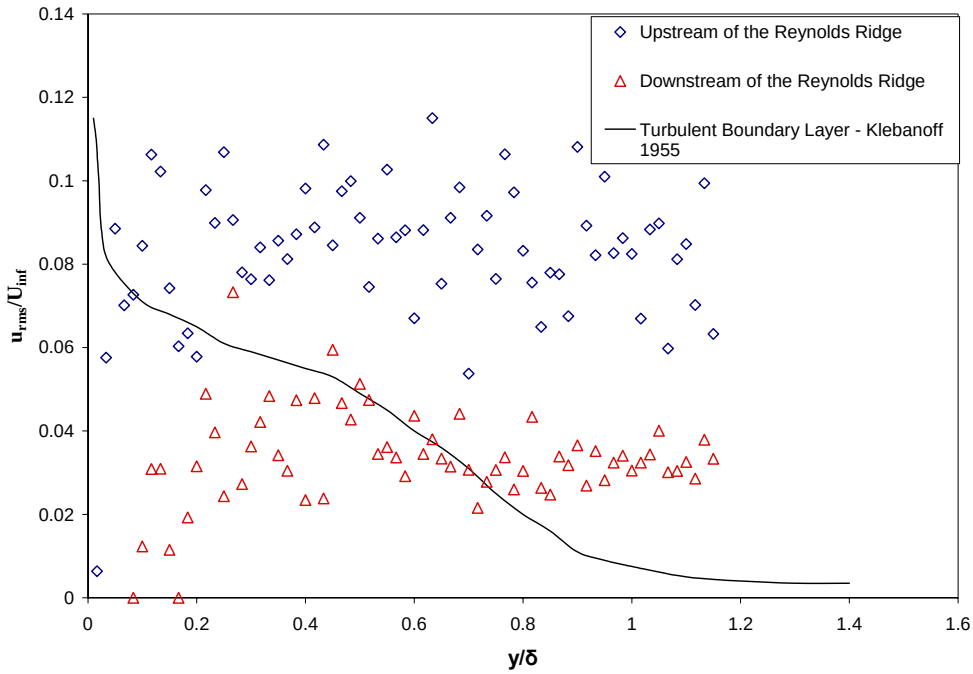

Figure 4.1.4: u_{rms} Profiles Upstream and Downstream of the Reynolds Ridge at $Re_L = 1.2 \times 10^5$. The standard deviations for upstream and downstream of the ridge are .017 and .01.

The boundary layer on the bubble upstream of the Reynolds ridge shows a slip-like condition compared to the profile downstream of the ridge and the Blasius profile. The profile downstream of the ridge is similar to the Blasius profile suggesting that the flow over the surfactant is near laminar. The u_{rms} is twice as large upstream of the ridge as downstream of the ridge. It is possible that the large variation in RMS velocity measurements is due to unsteadiness from surface

waves on the bubble surface below. The standard deviation of the u_{rms}/U_{inf} curves are 0.017 upstream and 0.01.

As the tunnel freestream velocity was increased, the bubble surface at the upstream edge of the bubble formed surface-like waves, yet, surprisingly, the bubble did not detach from the cavity until the highest freestream velocity of 0.4 m/s. The onset of the wave-like structures occurred at a freestream of about 0.3 m/s. At this freestream speed, the waves were two-dimensional. At higher freestream velocities, about 0.35 m/s, the large the waves at the front of the bubble became more pronounced and developed three-dimensional instabilities.

4.2 Bubble Production from Electrolysis

In practice, it is not feasible to hold a single large bubble on the hull of a ship. The large bubble tested on the acrylic plate only stayed in the cavity because the bubble was beneath a horizontal plate. In general, there is a size limit associated with bubble detachment from a cavity (Sections 2.4.4 and 2.4.5). However, it may be possible to approximate the large bubble surface coverage with thousands of smaller bubbles.

Smaller bubbles were produced via electrolysis on the forward drilled aluminum bubble plate while U_{inf} was set equal to zero. The acrylic plate was mounted to the force balance and oriented vertically in the water tunnel. Both voltage and current were monitored as the electrolysis process was studied.

At first, fifteen volts were applied to aluminum plate, and the leading edge of the mesh anode was place against the tunnel wall approximately 16 inches from the leading edge of the acrylic plate. Most of the bubbles did not grow and detach, but rather their growth gradually slowed until the growth could not be noticed by eye. Figure 4.2.1 shows the measured current as a function of time. At 30 seconds, the voltage was turned on.

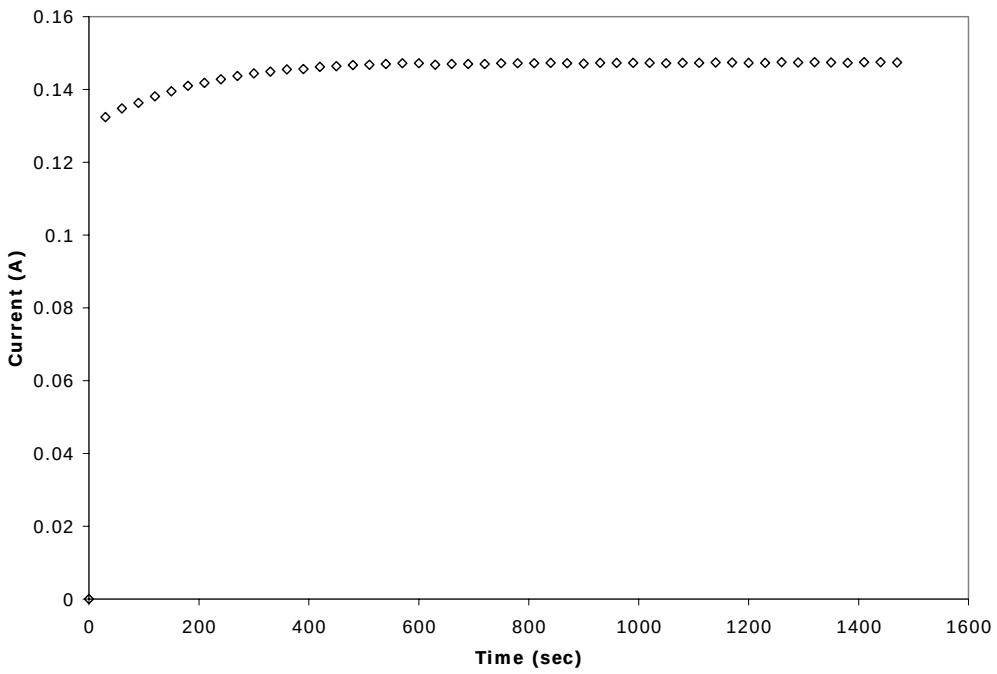

Figure 4.2.1: Current vs. Time using 15 Volts Applied between the Anode and Cathode

Initially after the voltage was applied, the current increased. However, after approximately 250 seconds, the current increase began to slow and then flatten

after approximately 600 seconds. The bubble growth was noticeable during the first 250 seconds, but as the current flattened, the bubble growth slowed and eventually looked as if the growth stopped. It is possible that the current did not saturate, and that both the current and bubble size were still increasing very slowly. The growth may have slowed because as the surface area of the bubble increased, the diffusive loss of hydrogen into the water increased. Eventually, the diffusive loss may equal the generation rate, and the bubble would stop growing. After 1500 seconds, the voltage was turned off and the resulting bubbles were observed. The electrolysis produced nearly spherical bubbles that extruded into the flow (Figure 4.2.2).

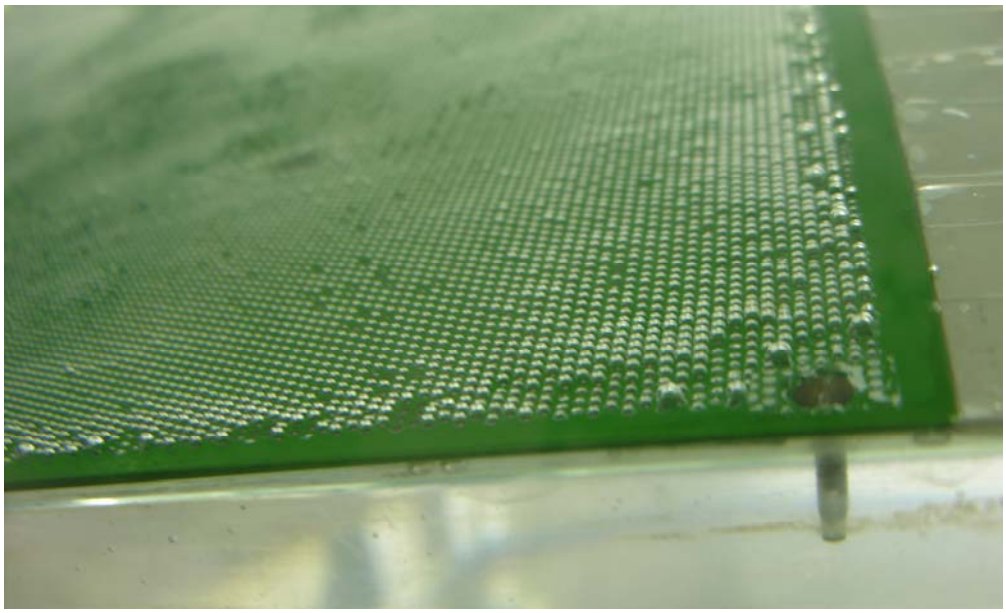

Figure 4.2.2: Bubbles Produced on the Aluminum Bubble Plate

The bubbles, however, were not uniform in size. Bubbles on the periphery of the aluminum plate were larger than the bubbles near the center of the plate.

The location of the mesh also influenced the growth of the bubbles. Bubbles in the holes closer to the anode grew faster and reached a larger size before the current saturated. When the mesh was placed downstream of the bubble plate, the holes toward the back of the plate produced the largest bubbles, and when the mesh was upstream, the bubbles at the front were largest. Bubbles were produced most uniformly when the mesh was placed at the same location as the bubble plate, but still the bubbles near the periphery were larger. If the mesh was placed closer to the bubble plate, the measured current was larger, and the bubbles grew faster and reached a larger size before the current saturated. Presumably, the bubble growth pattern reflects the local electric field intensity.

In addition to the location of the mesh anode, the bubble production process depends on the voltage applied to the plate. At higher voltages, the measured current was larger. With the anode located on the wall of the tunnel directly across from the forward-most aluminum bubble plate, the current saturated at about 0.1 A for 10 V and 0.19 for 15 V. At higher voltages, the bubbles grew faster and reached a larger size before the current saturated.

Bubble detachment was also observed at Reynolds numbers based on the length of the acrylic plate ranging from 1×10^5 to 4×10^5. Over this range of

Reynolds numbers, the vast majority of the bubbles remained in the cavities. In general, the bubbles that detached were the larger bubbles on the periphery of the aluminum bubble plate. The bubbles near the center of the plate did not detach. At low Reynolds numbers, a bubble would detach about every 30 seconds. At higher Reynolds numbers, a bubble would detach every few seconds.

The electrolysis also caused the aluminum plate to corrode. Even with the corrosion precautions detailed in Section 3.4.3, a white powdery layer began to build up in the holes near the periphery of the aluminum plate after a few hours of total electrolysis time. The stainless steel mesh anode, however, did not show any significant corrosion.

4.3 Drag Reduction due to Trapped Bubbles

The drag on the bubble plate was measured both with the force balance and from integrating the wake profile taken with the LDA. Drag was measured on the acrylic plate for three plate configurations. To test a solid flat plate, a steel perforated plate was inserted into the mounting cavity, and tape was applied to cover the holes creating, in effect, a solid flat surface. Thereafter, two bubble plate configurations were tested. For both bubble plate configurations, only the forward-most of the three aluminum plates had holes. Drag was measured on the entire acrylic plate both with and without bubbles trapped in the cavities. Bubbles were removed when necessary using a water jet to spray the holes. Each drag

value measured with the balance is a time-averaged sample of 2000 samples taken at a frequency of 100 Hz. Three such drag samples were taken at each test condition and averaged. The wake profiles were taken three inches from the trailing edge of the acrylic plate. At each Reynolds number, wake surveys were taken at the centerline of the plate and at locations 4 inches and 8 inches spanwise from the centerline.

4.3.1 Effect of Angle of Attack on Drag Measurements

The force balance was designed to allow for angle of attack adjustments to the plate. The angle of attack, α, was zeroed by measuring the width of the tunnel at the strut locations and centering both mounting struts. However, an angle of attack survey was taken to determine the exact zero angle of attack where the lift force should be perpendicular to the force measurement direction. If the plate is angled slightly, a component of the lift force will influence the drag measurement. Figure 4.3.1 shows the drag measured for each angle of attack over a range of Reynolds numbers based on plate length, Re_L.

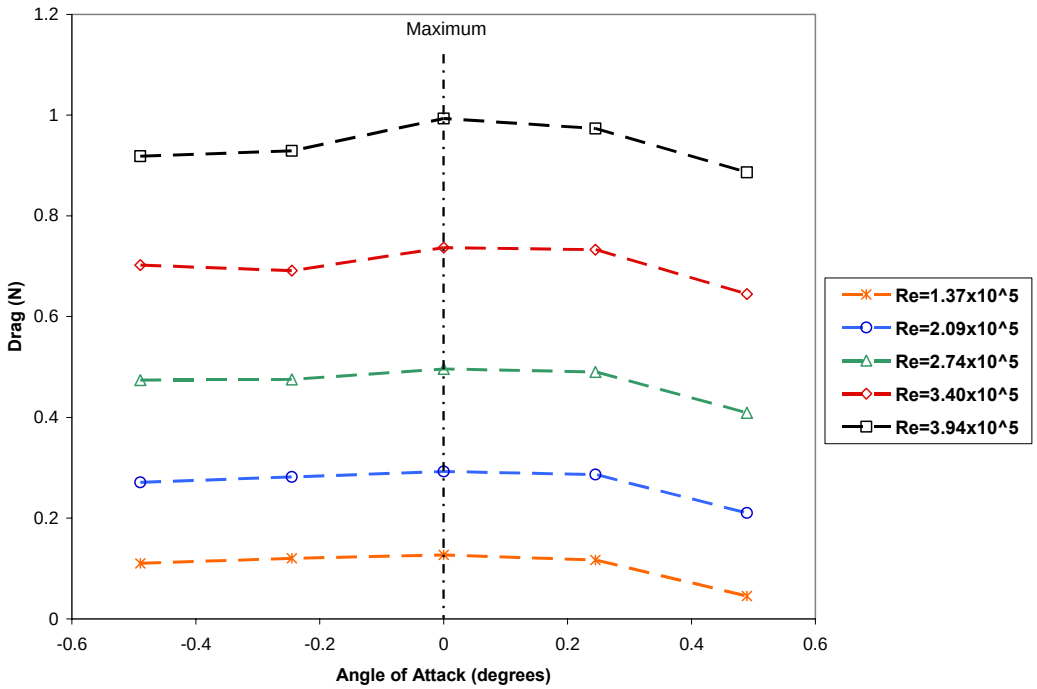

Figure 4.3.1: Drag Measured at Angles of Attack over a Reynolds Number Range

The zero-lift angle of attack corresponds to a drag maximum because the force balance measures the force along the centerline of the plate. At positive and negative angles of attack, the direction of the lifting force is defined to be perpendicular to the freestream direction, and thus a component of the lift influences the drag measured along the axis of the plate. The drag maximum for each Reynolds number occurred at $\alpha = 0°$. All subsequent drag measurements were thus taken at $\alpha = 0°$.

4.3.2 Drag Reduction over a Range of Reynolds Numbers

The force balance drag was measured for all three test cases, and wake surveys were taken for the two bubble plate configurations only. All drag results were compared to the analytic drag on a flat plate. The analytic drag was calculated by summing the drag due to turbulent boundary layers over both sides of the plate, the drag from the boundary trips, and the drag from the exposed flexures between the fairing and the plate (Appendix B.1). Figure 4.3.2 shows the drag over a range of Re_L for each plate configuration.

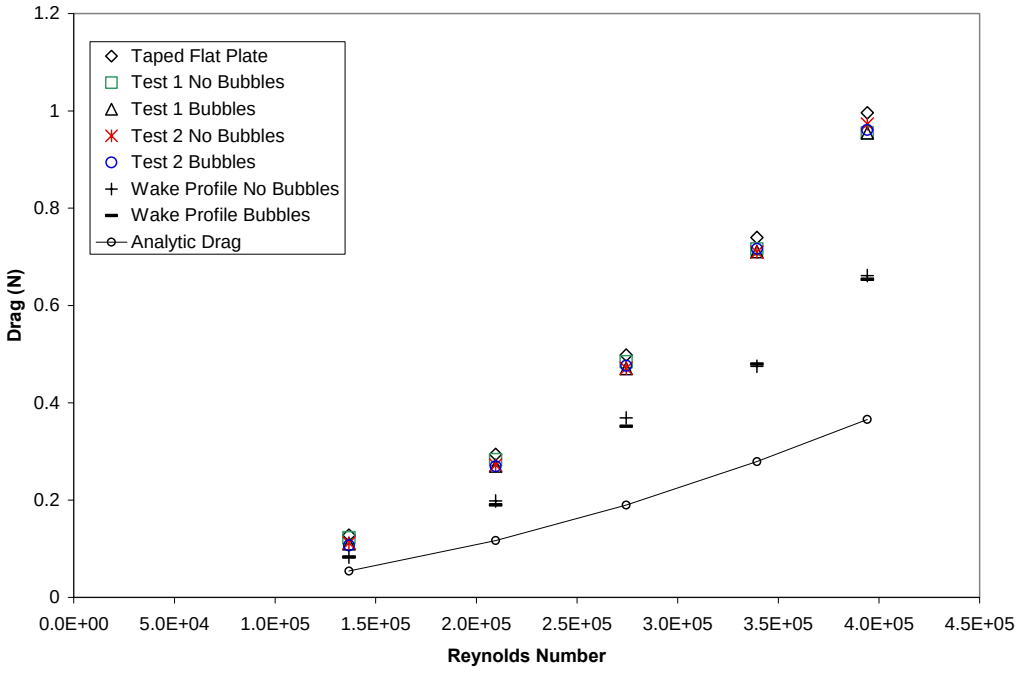

Figure 4.3.2: Drag Results Measured from the Force Balance and Wake Surveys. Tests 1 and 2 are repeated runs on different days.

As expected, the theoretical drag was more than 50-60% lower than the experimental drag. The higher experimental drag is expected to be from the drag caused by end effects from the boundary layer on the bottom of the tunnel and surface waves on the surface of the water in the test section. The bubble plates with and without bubbles showed a slightly reduced drag from the presumably flat plate case. That drag reduction is most likely a result of surface inconsistencies on the taped flat plate. The tape on the flat plate was not completely uniform—there were areas where the tape overlapped and the edge of the tape added roughness to the surface.

A better indicator of effect of the bubbles is to compare the drag measurements on the bubble plate with and without trapped bubbles. The drag on the bubble plate without bubbles was measured first. Bubbles were then electrolyzed in the holes, and when the current appeared to saturate, the voltage was turned off and the drag was measured. The plate configuration without bubbles was tested first because the process of removing bubbles from the holes with the water jet would change the internal stress in the force balance. Therefore, the force balance would not need to be re-calibrated prior to testing the plate with bubbles. Also, the buoyancy from the bubbles is assumed to be very small and to have negligible effect on the calibration of the plate. Drag was measured at Re_L of 1.37×10^5, 2.09×10^5, 2.74×10^5, 3.40×10^5, and 3.94×10^5.

The drag over the range of Reynolds numbers was measured twice on different days for repeatability (Tests 1 and 2). The bubbles produced on the plate during each test run were slightly different even though the anode was placed in the same location, across from the bubble plate, both times. For Test 1, the bubbles covered nearly all, about 99%, of the holes and the non-uniformity between the bubbles on the periphery and the bubbles near the center was small. For Test 2, the holes near the center of the bubble plate were covered entirely of bubbles, but several areas of 5-10 holes near the periphery of the bubble plate did not produce any bubbles. Overall, approximately 5% of the holes were not covered. Also, the non-uniformity of the bubbles was more evident than Test 1, which may have accounted for the poorer results. Table 1 shows the drag measurements and percent drag reduction at each Reynolds number for both runs. A positive percent drag reduction is a net decrease and a negative value is a net increase.

Table 4.3.1: Summary of Drag Measurements from the Force Balance

	Test 1			**Test 2**		
Re	No Bubbles (N)	Bubbles (N)	Percent Decrease (%)	No Bubbles (N)	Bubbles (N)	Percent Decrease (%)
1.37E5	0.123	0.110	10.3	0.112	0.107	4.5
2.09E5	0.283	0.270	4.5	0.272	0.270	0.9
2.74E5	0.484	0.470	2.8	0.471	0.476	-1.1
3.40E5	0.716	0.711	0.7	0.709	0.717	-1.0
3.94E5	0.955	0.955	0	0.973	0.961	1.2

The amount of drag reduction tended to decrease as Reynolds number increased. At Re_L of 1.37 x 10^5 and 2.09 x 10^5, both runs showed a drag reduction. However, at Re_L of 2.74 x 10^5, 3.40 x 10^5, and 3.94 x 10^5, the two runs did not agree. Test 1 showed similar drag at Re_L of 3.94 x 10^5. Test 2 showed drag increases at Re_L of 2.74 x 10^5 and 3.40 x 10^5, and a drag decrease at a Re_L of 3.94 x 10^5. The difference between the crossover points from drag decrease to increase for the two runs may have been due to the non-uniformity in bubbles. The bubbles produced in Test 2 may have been larger than those in Test 1. The larger bubbles could have influenced the net drag measurement. The slight drag decrease for the highest Reynolds number in Test 2 may have been a result of the larger bubbles detaching from the cavities, and thus decreasing the overall pressure drag. Obviously, however, more testing would have been beneficial.

Because the absolute drag measurements may be slightly off, this study focuses on relative changes. The error associated with the strain gages themselves is quite small, approximately 1%. However, the internal stress of the force balance may change slightly over the course of each test. Changes in the internal stress are most likely caused by the screw joint between the strut and the flexure. Although the screws appear tight, as the flexures deflect parallel to the flow, the joint is not as rigid in the orthogonal direction perpendicular to the flow. Therefore, any lift from the plate may change the internal stress of the balance.

To determine this error induced by the lift, a calibration curve was taken, the plate was subjected to the entire range of flow speeds, and a calibration curve was taken again. The difference between the two calibration factors was about 2%.

Drag was also calculated from a momentum balance by integrating the wake profiles. The calculation assumes a 2-D, steady, zero pressure gradient flow. Because the hole coverage is small, the expected drag reduction is also small. Therefore, the difference in wake profiles of the plate with and without bubbles cannot be distinguished visually (Figure 4.3.3).

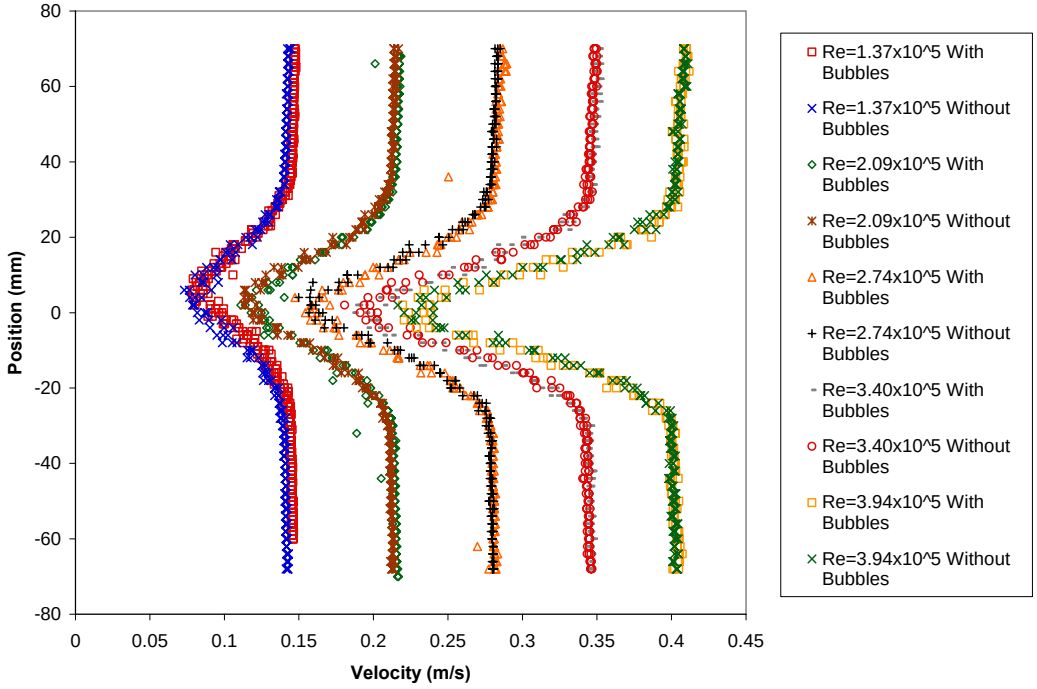

Figure 4.3.3: Wake Profiles 3 inches behind Test Plate

Table 4.3.2 shows the calculated drag from the wake surveys with and without bubbles on the bubble plate. Similar data are shown in Figure 4.3.2 for the drag measured by the force balance.

Table 4.3.2: Summary of Drag Measurements from the Wake Survey

Re	No Bubbles (N)	Bubbles (N)	Percent Reduction (%)
1.37E5	0.083	0.083	0.0
2.09E5	0.198	0.190	4.0
2.74E5	0.369	0.352	4.6
3.40E5	0.475	0.480	-1.0
3.94E5	0.661	0.654	1.1

The calculated drag from the wake survey is smaller than the drag measured by the force balance because the integrated wake method does not include the drag on the flexures and end effects of the plate. The wake profiles show slightly reduced drag at Re_L of 2.09 x 10^5, 2.74 x 10^5, and 3.94 x 10^5 and unchanged or increased drag at Re_L of 1.37 x 10^5 and 3.40 x 10^5. The drag difference calculated by the wake survey approach differs from the drag difference measured by the force balance. The source of the discrepancy could be due to small inconsistencies between the tunnel freestream settings for the wake survey and force balance measurements, or because of significant bubble diffusion over the course of the wake data acquisition, approximately 45 minutes. Also, the drag reduction may be too small for this preliminary wake survey to accurately resolve. The drag results at the lowest Reynolds number is probably flawed because the

difference between freestream velocities for the wake profiles taken with and without bubbles was about 3%.

4.3.3 Effect of Voltage on Drag Measurements

The voltage applied to the plate caused electrical interference and affected the force measured by the strain gages. Figure 4.3.4 shows the force and current readings recorded every minute for Re_L of 2.09×10^5.

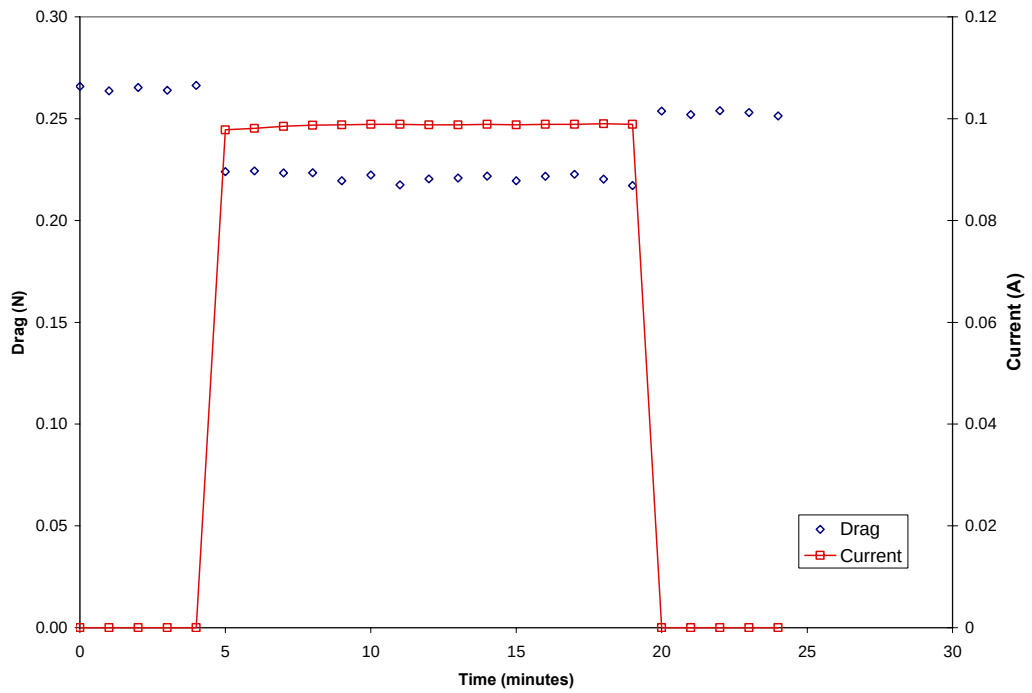

Figure 4.3.4: Drag and Current during Electrolysis with Constant Voltage

Initially, the plate had no bubbles trapped in the cavities. The mesh was placed along the wall of the tunnel across from the forward-most bubble plate. After four minutes, 10 volts were applied to the plate, and after nineteen minutes the voltage was turned off. The measured drag decreases approximately 15% when the voltage is turned on. However, the final drag measurement with the voltage turned off is only about 5% less than the initial drag measurement prior to applying voltage. This is consistent with the drag change measured by the force balance in Test 1 and the drag change from the wake survey. When the voltage is turned on, the electrolysis circuit seemed to cause electrical interference with the force balance. It is possible that voltage may have leaked into the strain gage circuit through contact between the electrically charged water and aluminum flexure. Hence to ensure reliable drag measurements, current to the plate is turned off during each drag measurement.

4.3.4 Drag Measurements During Bubble Growth

At Re_L of 2.09×10^5, drag was then measured over a time period as the bubbles grew from electrolysis. Because applied voltage caused electrical interference, fifteen volts were applied at set intervals but turned off during drag sample periods. Initially, the voltage was on for thirty-second intervals, but as the current reached its saturation point, the intervals were extended to one minute. Again, the mesh was placed flush on the tunnel wall across from the forward-most

bubble plate and was not removed during the sampling. Figure 4.3.5 shows the drag and current as a function of time.

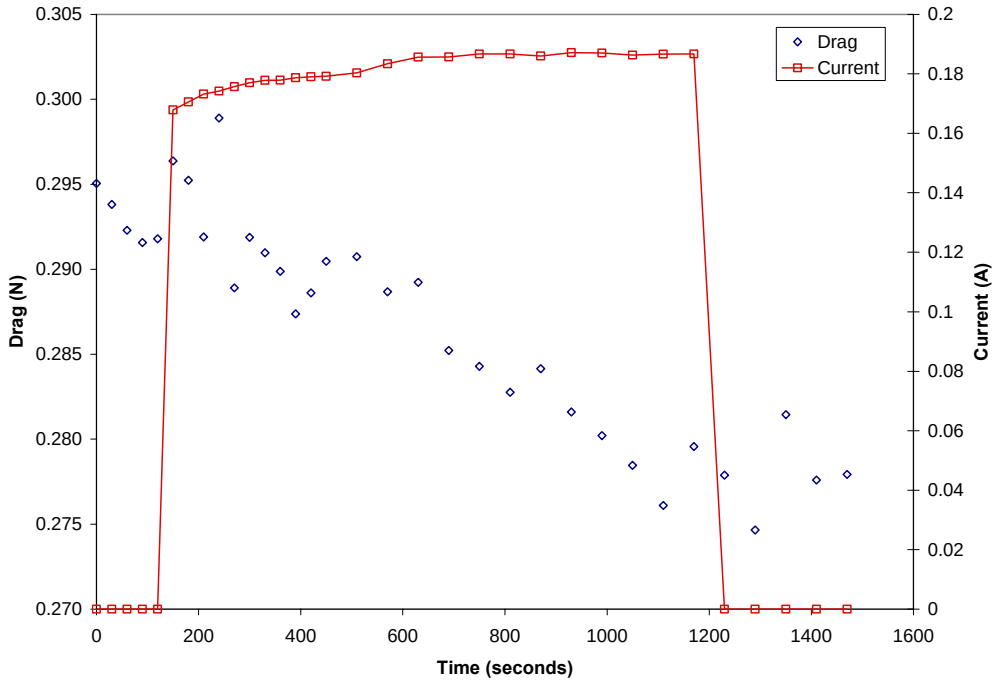

Figure 4.3.5: Drag and Current during Electrolysis with Voltage Turned off during Drag Sampling

The time scale represents time while the voltage is on. Time during the drag sampling is not shown. Initially after the voltage is turned on, the measured drag briefly increases. However, it was possible that the plate was not allowed to stabilize completely—when conditions change, the plate takes time to settle—before taking these readings. Yet, over the subsequent electrolysis period, the drag showed a generally consistent decreasing trend. The drag decreased

approximately 5% over the electrolysis period, the total change is similar to that shown in Figure 4.3.4. Again, the drag reduction is consistent with Tests 1 and 2.

4.4 Boundary Layer Measurements

Boundary layer measurements were taken at freestream tunnel speeds of 0.14 m/s and 0.21 m/s with a LDA. At a freestream of 0.23 m/s, contour plots of streamwise velocity were taken perpendicular to the flow along the span of the plate at three locations—just upstream of the bubbles, on the bubbles, and just downstream of the bubbles. The velocity data at each location was span-averaged and the resulting velocity profiles were compared. At a freestream of 0.12 m/s, one-dimensional profiles with higher spatial resolution were taken over the bubbles and compared to the profile measured on the opposite solid side of the plate. For these LDA surveys, the plate was mounted vertically in the tunnel and spacers were wedged beneath the plate lower edge and the tunnel wall to reduce the plate oscillations.

4.4.1 Boundary Layer Contours and Profiles

Figure 4.4.1 shows the velocity contour taken upstream of the first row of bubbles. The origin of the plot is 5.5 inches from the leading edge and about 5 inches from the bottom edge of the plate. This location corresponds to a Reynolds number based on streamwise location, Re_X, of 3.21×10^5. The positive

direction for the span axis, *z*, is upward toward the top of the tunnel and is normalized by the plate width, *w*. *y* is normalized by $\delta = 7$ mm.

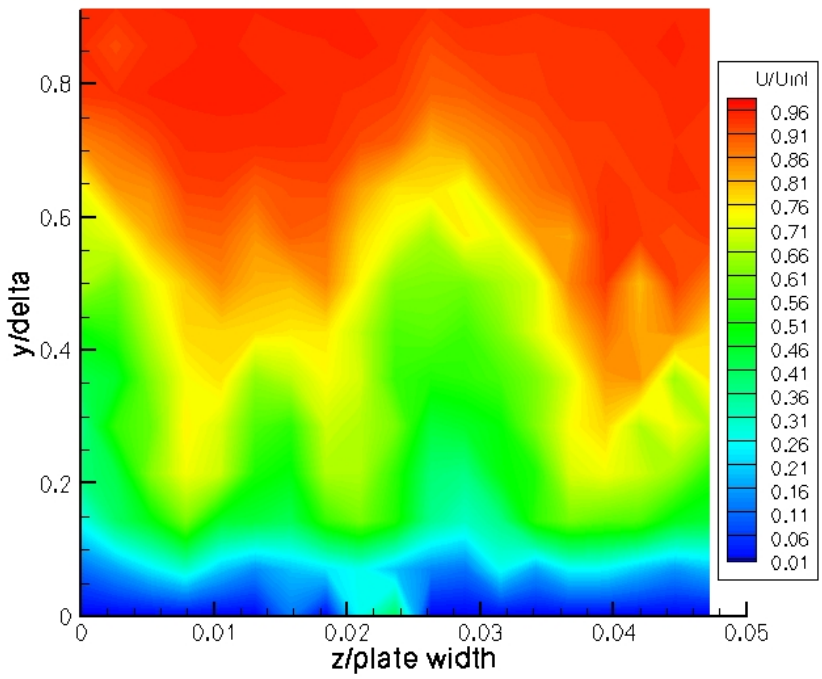

Figure 4.4.1: Velocity Contour Upstream of the Bubbles

Natural transition to turbulent flow on a smooth plate would be expected to occur at a critical Reynolds number, Re_{crit}, of about 3×10^5. However the boundary layer is tripped, and as expected, the wake of the boundary trips is clearly seen at spanwise locations near *z/w* of 0.0 and 0.026. A low velocity bulge is also evident at *z/w* of .012. It is unclear what causes this bulge, but the bulge is not a wake of

a boundary layer trip because the boundary trips are space approximately one centimeter apart. The low velocity bulge could be a result of surface roughness upstream or may be part of a low speed streak forming between trips. A second velocity contour was taken over the bubbles at Re_X of 8.45 x 10^5 (Figure 4.4.2). The location of the second plot is the same as the first plot location, but translated downstream 14.5 inches from the leading edge. The y-axis is normalized by δ = 12 mm.

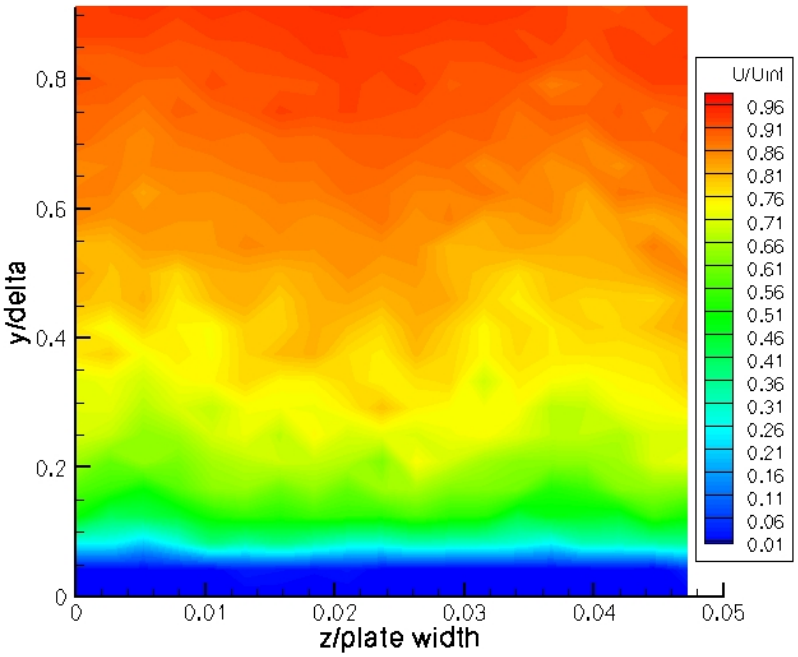

Figure 4.4.2: Velocity Contour over the Bubbles

At this location, individual wakes of the boundary trips are less clear. There are slight bulges near *z/w* of 0.004 and 0.036, but overall, the boundary layer is generally uniform spanwise. Also, the boundary layer thickness over the bubbles is approximately twice the thickness just upstream of the bubbles. The final velocity contour was taken at Re_X of 9.33 x 10^5 or 16 inches from the leading edge (Figure 4.4.3). Here, the y-axis is normalized by δ = 15 mm.

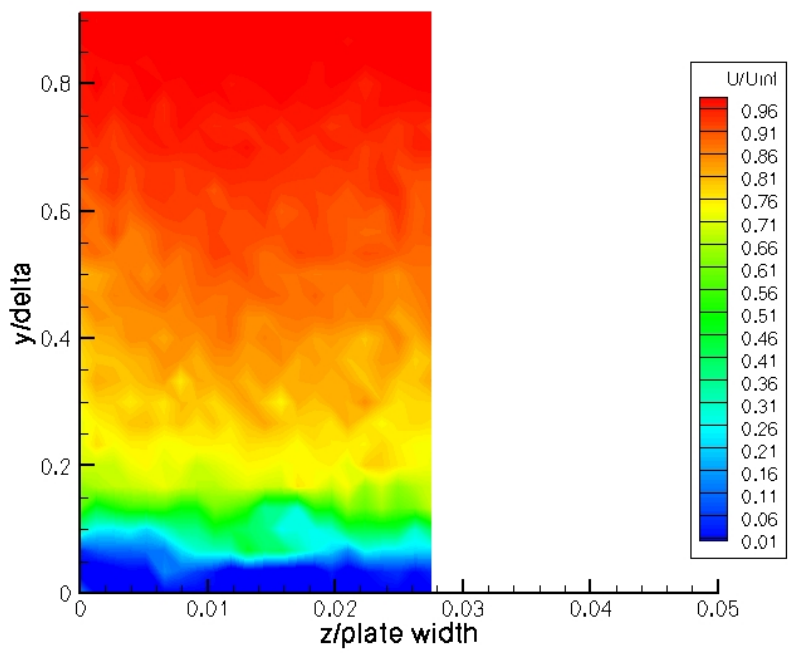

Figure 4.4.3: Velocity Contour Downstream behind the Bubbles

This plot is oriented similarly to the previous plots except that the span of the data taken is reduced in half. Here, the effect of the bubbles is generally uniform across the span of the plate.

Transition along the plate is difficult to quantify from the contour plot. Therefore, the velocity contours are span-averaged at all three streamwise locations, and the one-dimensional profiles are compared to the analytic turbulent boundary layer model based on the $1/7^{th}$ power law (Figure 4.4.4). RMS velocity profiles are plotted as well (Figure 4.4.5). The velocity and position are plotted as non-dimensional values, where the mean velocity, U, is divided by the freestream velocity, U_{inf}, and the distance away from the plate surface, y, is divided by the boundary layer thickness, δ. The boundary layer thickness is generally determined by the location where the velocity is 99% of the freestream velocity. However, the profiles taken over the bubble and downstream of the bubble did not extend far enough into the freestream, and the last data point was assumed to be δ. The profiles over the bubbles are compared to a boundary layer profile on the flat side of the plate was taken at Re_X of 8.45×10^5. Because the bubbles extrude into the flow, it is unclear whether to reference the actual plate surface or the top of the bubble. Therefore, two analytic curves are presented. One is referenced from the surface of the actual plate, and the other is referenced from the approximate height of the bubbles.

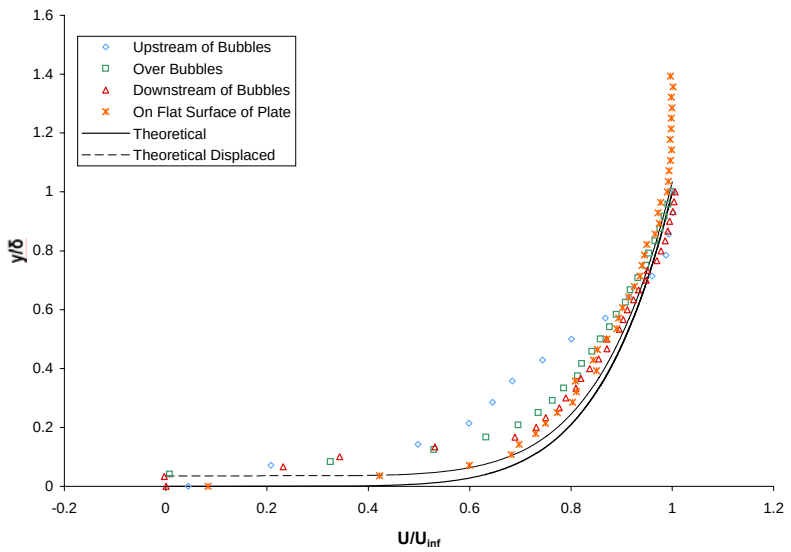

Figure 4.4.4: Span-Averaged Velocity Profiles in the Boundary Layer

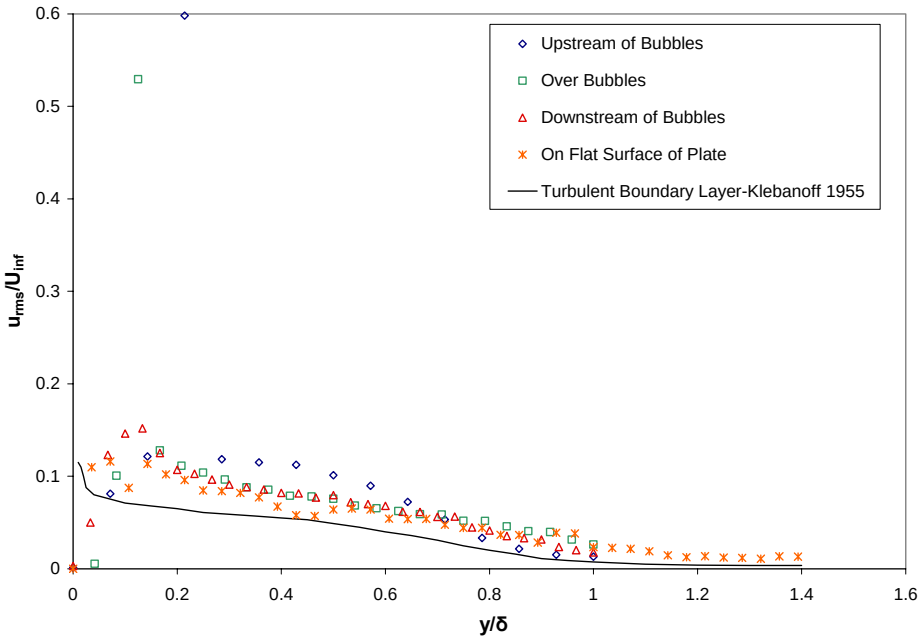

Figure 4.4.5: Span-Averaged RMS Streamwise Velocity Profiles in the Boundary Layer

At this Reynolds number, the viscous length scale, l^*, is and the 2 mm bubble is twice as large as the than l^* (Appendix B.2). The development of the tripped boundary layer is observed. At all three Re_X, the boundary flow has begun to transition, but is not yet fully turbulent. At Re_X of 3.21 x 10^5, the profile shows an inflection point around y/δ of 0.3 corresponding to the boundary trip wake. The RMS velocity plot also shows the boundary trip effect between y/δ of 0.3 to 0.7. Further downstream at Re_X of 8.45 x 10^5, there is no inflection point implying that the individual wakes of each boundary trip have merged. Here the measured profile resembles the analytic turbulent profile, but the velocity gradient near the surface is slightly smaller, and the measured profile is not quite as full. None of the profiles suggest an obvious induced slip-like condition on the bubble surface like that seen earlier on the single large bubble (Figure 4.1.3).At a Re_X of 8.45 x 10^5, the velocity profile over the bubbles is compared to the profile over the flat surface on the other side of the plate. The bubble profile is slightly displaced due to the height of the bubble. However, the two profiles merge at $y/\delta > 0.7$. The RMS velocity profiles over the bubble and on the flat surface are quite similar. Both have maximum values near $y/\delta = 0.15$. Finally, because the flow has not yet fully transitioned, it may be difficult to isolate the effect of the tiny bubble surface. For a better comparison to an analytic turbulent boundary layer, profiles should have been taken further downstream on a larger bubble-covered

surface, but the test plate did not have any bubbles downstream because the aft two aluminum plates had not yet been drilled.

4.4.2 Fine Resolution Survey of a Laminar Boundary Layer

Because the slip condition may be difficult to see clearly in a transitioning flow, boundary layer profiles were taken at lower tunnel speeds in the laminar flow regime. High resolution boundary layers were taken on both sides of the acrylic plate at Re_L of 9.53 x 10^5 (Figure 4.4.6 and 4.4.7).

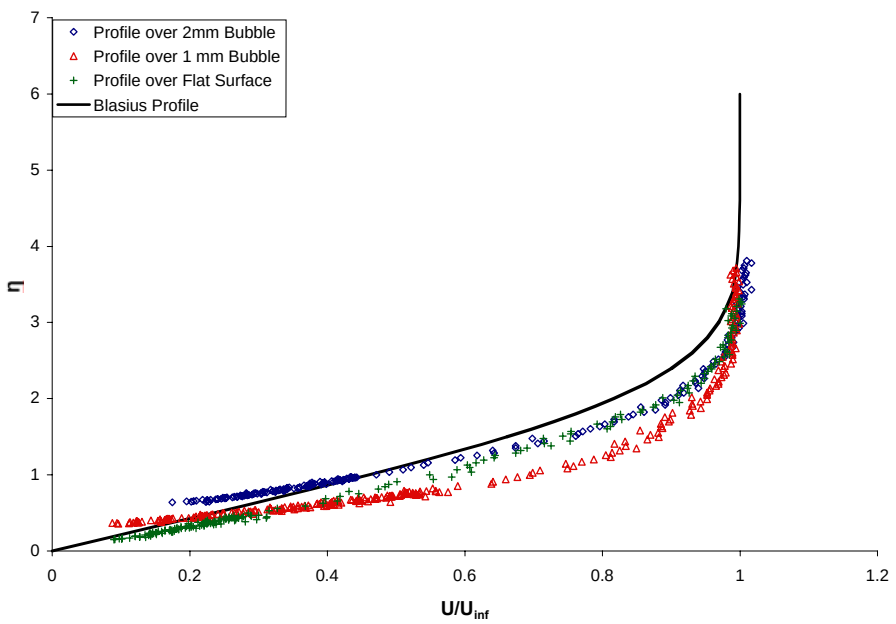

Figure 4.4.6: High Resolution Velocity Profiles at Re_X of 3.95 x 10^4

On the bubble side, a boundary profile was taken over a single approximately 1 mm bubble surrounded by bubbles of similar size r. A second profile was taken over an isolated bulging two-millimeter diameter bubble that was much larger

than the surrounding bubbles. A third profile was taken on the solid side of the flat plate for comparison to the profiles over the bubbles. All three profiles were taken about 13 inches from the leading edge or Re_X of 3.95 x 10^4 with 0.01 mm resolution of the traverse near the surface and 0.1 mm resolution throughout the rest of the boundary layer. The velocity, non-dimensionalized similar to the previous boundary layer plots, is plotted with respect to the similarity variable. The RMS velocity is plotted with respect to y/δ.

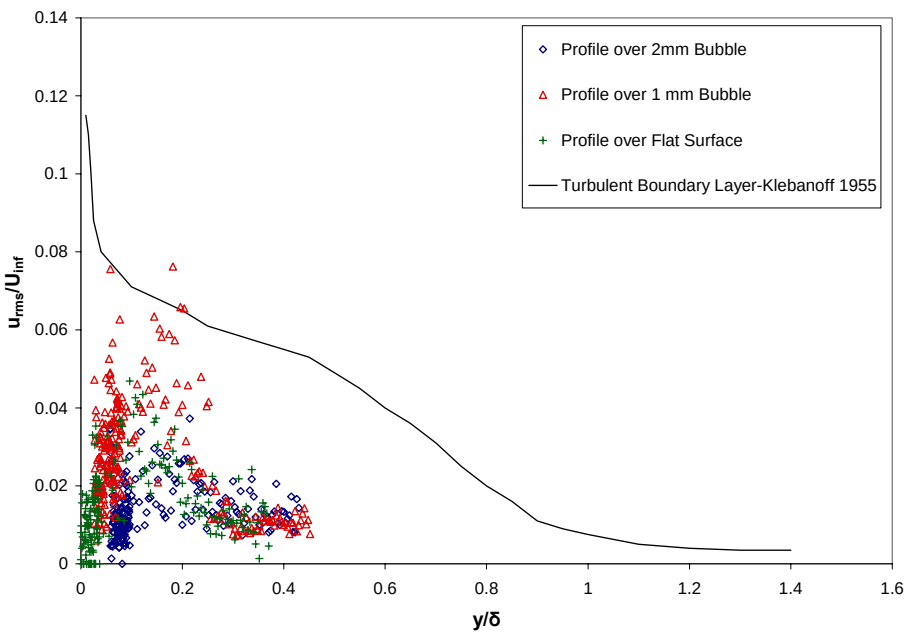

Figure 4.4.7: High Resolution RMS Velocity Profiles at Re_X of 3.95 x 10^4. Standard deviation for 2mm bubble = 0.007, 1mm bubble = 0.013, Flat Surface = 0.010.

The measured profiles compare reasonably well with the Blasius profile. The differences may be due to the elliptical leading edge of the plate and the boundary trips. It is unclear if the profiles again exhibit a clear slip-like condition on the bubble surface. At this low Reynolds number, surfactant may have built up on the bubbles. The bubble interface not only then becomes a no-slip boundary, but the bubbles themselves may act as roughness resulting in a larger shear rate. Even if the bubbles are not fully contaminated, surfactant likely builds up at the back of the bubble. Assuming the bubbles are on average one millimeter in diameter, only a fraction of a square millimeter of the bubble surface may be clean. Therefore, because the width of the LDA probe volume is approximately 0.5 mm, the LDA may not have sufficient resolution to independently measure the velocity on the clean surface from the contaminated surface. The profiles also show that the velocity near the outer portion, $y/\delta > 0.6$, of the boundary layers seems to be unaffected by the presence of the bubbles. Both profiles over the bubbles begin at the surface of the bubble, which is displaced a couple millimeters from the plate surface. However, all three profiles collapse onto the same curve in the outer part of the boundary layer. The RMS velocities of the three cases are much less than the turbulent RMS velocities suggesting that the flow is nearly laminar at this Reynolds number. The u_{rms} over the 1 mm bubble is slightly higher than over the 2 mm bubble and flat surface suggesting that the effect of a group of bubbles is

different than the effect of an isolated bubble, or that there was very slight movement of the plate during testing.

Chapter 5

Conclusions

5.1 Bubble Production and Contamination

As a preliminary study to examine the effect of surfactant and the boundary condition on a bubble surface, a large bubble was injected in the empty cavity beneath the horizontally mounted acrylic plate. A Reynolds ridge formed on the bubble surface. Upstream of the ridge, the bubble surface was clean and the boundary layer profile showed a slip-like boundary condition. However, downstream of the ridge, the bubble surface was contaminated and the profile showed a no-slip-like mean boundary condition although there was still particle motion in the fingers. As surfactant built up on the bubble, the ridge moved upstream.

The bulk of the study concerned the effect of a dense population of small bubbles trapped on the surface of a plate. In this study, groups of small bubbles

were produced in cavities via electrolysis. Bubble growth and occasional detachment were observed. Bubbles growth was found to depend on location of the anode and the amount of voltage applied to the plate. Bubbles grew faster and reached a larger size if the anode was located closer to the bubble plate and if higher voltages were applied because both presumably increase local electric field strength. In general, the bubbles were not uniform in size. The bubbles near the periphery of the bubble plate were slightly larger than the bubbles near the center of the plate. Very few bubbles detached at the highest Reynolds number flows.

5.2 Drag Reduction

The bubble effect on drag was measured with a force balance and wake surveys. Relative drag changes between the bubble plate with and without bubbles were observed over a range of Re_L between 1×10^5 and 3×10^5. In general, the drag reduction decreased as Re_L increased. The highest drag reduction of 10% occurred at the lowest Re_L, while small drag increases may have occurred at several of the higher Re_L cases. The absolute drag reduction was not shown to be repeatable—the drag reduction for two separate tests differed by more than 50% at each Reynolds number. The disagreement may be related to the non-uniformity of the bubbles because the size of the bubbles may have been different for each test. Also, the force balance error is about 2-3%. With only 7-

8% bubble coverage of the entire plate, the error becomes significant. The percent drag reduction from the wake surveys did not agree with the reduction measured with the balance, but they were close. However, the wake survey does not account for the end effects from the finite plate.

The effect of the bubbles upon drag is more clearly seen when drag and current were measured as a function of time as the bubbles were produced via electrolysis. At Re_L of 2.09 x 10^5, the drag decreased as the bubbles grew. Even, after the current appeared to saturate, the drag still decreased. The drag decreased about 5 % over the test period. At this Re_L, the 5% drag reduction was consistent with the reduction found from both the force balance and the wake survey.

The net power saved is determined by comparing the power required to drive the plate to the power required to electrolyze to bubbles. At Re_L = 2.09 x 10^5, the power required to drive the plate is about 0.06 W. If the applied voltage is 10 V and the resulting current is about 0.1 A, the total power for electrolysis is 1 W (Appendix B.3). Assuming a 5% drag reduction, the power saved is smaller than the electrolysis power. However, the plate was not fully covered with bubbles. Also, the electrolysis is not continuous—the voltage is turned off after the bubbles are produced. Therefore, if the voltage is periodically pulsed, the bubble trapping system may be optimized to achieve net power savings.

5.3 Boundary Layer Profiles

Velocity profiles were taken in the boundary layer upstream of the bubbles, over the bubbles, and just downstream of the bubbles. The profiles showed that the bubbles affected the near-wall region, but not the outer region. However, the profiles taken over the bubbles did not show an obvious slip-like condition. It is possible that the LDA probe width is too large to sufficiently resolve the bubble surface. At this bubble scale, it is unclear if the bubble interface is indeed a slip-like surface.

5.4 Recommendations

From the observations in this study, a few changes may give better results for future work. A better estimate of the error may be obtained by computing calibration constants before and after each run. The drag measurements should be repeated as well. The drag measured during the bubble growth should be extended to see if the drag increases again over time as the bubbles diffuse into the water. More reliable drag results could also be obtained with more bubble coverage; future tests should complete drilling the other bubble plates increasing the bubble coverage. Other hole shapes may also be considered. Other metals, such as stainless steel, should be considered for the bubble plate because

aluminum corrodes too easily during electrolysis. Also, paint does not effectively adhere to aluminum even when pre-treated with self-etching solution and metal primer. The bubbles may be able to be produced more uniformly if the anode is embedded in the plate itself by manufacturing a tile-like plate where tiles of anode are surrounded by bubble cavities or a grid–like plate where anode strips are placed between bubble areas.

Appendix A

A.1 Kumar and Kuloor Bubble Model

The bubble models discussed here were developed by Kumar and Kuloor. The following model is for bubble growth and detachment from a horizontally oriented orifice in a static fluid. The model is based on two stages of bubble expansion. The first expansion stage ends when the buoyancy, gravity, and surface tension forces acting on the bubble are in equilibrium. The second stage ends when the bubble detaches. For an inviscid liquid with surface tension, the second-order approximation of the final bubble volume, V_F, at detachment is

$$r_0 = \frac{P}{4Q}\left(V_F^{\,2} - V_0^{\,2}\right) - \frac{J}{Q}\left(V_F - V_0\right) \qquad \text{(Eq A.1.1)}$$

where Q is the gas flow rate. The first stage radius, r_o, and volume, V_o, are determined from balancing the upward buoyancy force, the downward surface tension forces, and the downward expansion forces due to changes in momentum and the drag caused by the growing bubble as follows:

$$V_0 - \left(\frac{11Q^2}{192\pi(3/4\pi)^{2/3} g} \right) V_0^{-2/3} = \frac{\pi d_C \gamma \cos\theta}{\rho_l g}$$

(Eq A.1.2)

where g is the acceleration due to gravity, γ is the interfacial tension between the gas in the bubble and the surrounding liquid, and θ is the contact angle of the interface with respect to the solid surface. The P and J variables are substitutes for the expressions

$$P = \frac{(\rho_l - \rho_g) g}{Q[\rho_g + (11/16)\rho_l]} \qquad \text{(Eq A.1.3)}$$

$$J = \frac{\pi d_C \gamma \cos\theta}{Q[\rho_g + (11/16)\rho_l]} \qquad \text{(Eq A.1.4)}$$

ρ_g and ρ_l are the densities of the gas and liquid.

The bubble model for orifice orientations for non-horizontal surfaces is as follows. Following the same force balance methodology, the bubble model becomes

$$\left(r_0 \cos\phi + \frac{1}{2} d_C \sin\phi \right) = \frac{B}{2Q(A+1)} \left(V_F^{\,2} - V_0^{\,2} \right) - \frac{C}{AQ} (V_F - V_0) - \frac{3D}{2Q(A-1/3)} \left(V_F^{\,2/3} - V_0^{\,2/3} \right)$$

(Eq A.1.5)

where the initial volume is solved by

$$V_0^{5/3} = \frac{11Q^2}{192\pi(3/4\pi)^{2/3} g} + \frac{3\mu Q V_0^{1/3}}{2(3/4\pi)^{1/3} g\rho_l} + \frac{\pi d_C \gamma V_0^{2/3}}{g\rho_l}\cos\phi$$

(Eq A.1.6)

and the substitution variables are

$$A = 1 + \frac{7.5\pi(3/4\pi)^{1/3} V_0^{1/3}\mu}{Q\left[\rho_g + (11/16)\rho_l\right]} \qquad \text{(Eq A.1.7)}$$

$$B = \frac{(\rho_g - \rho_l)g}{Q\left[\rho_g + (11/16)\rho_l\right]} \qquad \text{(Eq A.1.8)}$$

$$C = \frac{\pi d_C \gamma \cos\phi}{Q\left[\rho_g + (11/16)\rho_l\right]} \qquad \text{(Eq A.1.9)}$$

$$D = \frac{3\mu}{2}\left(\frac{3\pi}{4}\right)^{1/3}\left(\rho_g + (11/16)\rho_l\right) \qquad \text{(Eq 2..1.10)}$$

The orifice orientation angle, ϕ, is measured with respect to horizontal.

Appendix B

B.1 Analytic Drag

The analytic drag is the summation of the drag on a turbulent flat plat, drag from the boundary trips, and drag from the exposed flexure. The drag coefficient, C_D, for a turbulent smooth-wall flow is

$$C_D \approx \frac{0.523}{\ln^2\left(0.06\,\mathrm{Re}_L\right)} \qquad \text{(Eq B.1.1)}$$

Where the Reynolds number based on plate length, $\mathrm{Re}_{L,\ is}$

$$\mathrm{Re}_L = \frac{U_\infty L}{\upsilon} \qquad \text{(Eq B.1.2)}$$

U_∞ is the freestream velocity, L is the plate length and v is the kinematic viscosity for water. Absolute drag, D, is calculated from the drag coefficient as follows:

$$D = \frac{1}{2}\rho U_\infty L b C_D \qquad \text{(Eq B.1.3)}$$

ρ is the density of water and b is the width of the plate. The drag from the boundary trips and exposed flexure is calculated in the same mater except that the drag coefficients are different. The drag coefficient of a boundary trip, $C_{D,trip}$, is

$$C_{D,trip} = \frac{24\upsilon}{U_{\infty}k} \qquad \text{(Eq B.1.4)}$$

where k is the trip height. The drag coefficient for an exposed flexure, $C_{D,flexure}$, is approximately 1.2 from experimental curve fits.

B.2 Viscous Length Scale

For a turbulent boundary, the viscous length scale, l^*, is defined as

$$l^* = \frac{\nu}{u^*} \qquad \text{(Eq B.2.1)}$$

u^* is the wall friction velocity and is defined as

$$u^* = \sqrt{\frac{\tau_w}{\rho}} \qquad \text{(Eq B.2.2)}$$

where τ_w is the wall shear stress.

B.3 Net Power Saving

The net power saving is determined from the electrolysis power and the power required to overcome the drag. The electrolysis power is simply the product of the applied voltage and current. The power required to overcome the drag is the product of the drag and freestream velocity.

References

Balasubramanian, A., Miller, A. C., Traub, L. W., and Rediniotis, O. K., "Biomimetic nanostructure skin for hydrodynamic drag reduction," AIAA Paper 2003-0785, 2003.

Bushnell, D. M., "Drag reduction 'Designer Fluid Mechanics' – Aeronautical status and associated hydrodynamic possibilities," AIAA Paper 97-2110, 1997.

Choi, K. S., "European drag-reduction research—recent developments and current status*," Fluid Dynamics Research*, Vol. 26, pp. 325-335, 2000.

Davis, J. R., Corrosion of Aluminum and Aluminum Alloys, ASM International, 1999.

Hoyt, J. W., "The effect of additives on fluid friction," *Trans. ASME: J. Basic Engineering*, Vol. 94, pp. 258-285, 1972.

Kodama, Y., Kakugawa, A., Takahashi, T., and Kawashima, H., "Experimental study on microbubbles and their applicability to ships for skin friction reduction," *International Journal of Heat and Fluid Flow*, Vol. 21, pp. 582-588, 2000.

Kumar, R., and Kuloor, N. R., "The formation of bubbles and drops," Advances in Chemical Engineering, Vol. 8, pp. 255-368, 1970.

Lucey, A. D., and Carpenter, P. W., "A numerical simulation of the interaction of a compliant wall and inviscid flow," *Journal of Fluid Mechanics*, Vol. 234, pp. 121-146, 1992.

Madavan, N. K., "Reduction of turbulent skin friction by mircobubbles," *Physics of Fluids*, Vol. 27, pp. 356-363, 1984.

Madavan, N. K., Deutsch, S., and Merkle, C. L., "Measurements of local skin friction in a microbubble modified turbulent boundary layer," *Journal of Fluid Mechanics*, Vol. 156, pp. 237-256, 1985a.

Madavan, N. K., Deutsch, S., and Merkle, C. L., "Numerical investigations into the mechanisms of microbubble drag reduction," *Journal of Fluid Mechanics*, Vol. 107, pp. 370-377, 1985b.

Marshall, S. H., Chudacek, M. W., and Bagster, D. F., "A model for bubble formation from an orifice with liquid cross-flow," *Chemical Engineering Science*, Vol. 48, No.11, pp. 2049-2059, 1993.

Matsumoto, M., and Matsuura, T., "Molecular dynamics simulation of a rising bubble," *Molecular Simulation*, Vol. 30, pp. 853-859, 2004.

McCormick, M. E., and Battacharyya, R., "Drag reduction on a submersible hull by electrolysis," *Naval Engineering Journal*, Vol. 85, pp. 11-16, 1973.

Migirenko, G. S., and Evseev, A. R., "Turbulent Boundary Layer with Gas Saturation," *Problems of Thermophysics and Physical Hydrodynamics*, 1974.

Nahra, H. K., and Kamotani, Y., "Prediction of bubble diameter at detachment from a wall orifice in a liquid cross-flow under reduced and normal gravity conditions," *Chemical Engineering Science*, Vol. 58, pp. 55-69, 2003.

Pal, S., Deutsch, S., and Merkle, C. L., "Bubble characteristics and trajectories in a microbubble boundary layer," *Physics of Fluids*, Vol. 31, pp. 744-751, 1988.

Pollard A., "Passive and active control of near-wall turbulence," *Prog. Aerospace Sci*., Vol. 33, pp 689-708, 1997.

Satterly J., and Turnbull R., "The ridge at the junction of clean and contaminated liquid surfaces," *T. Roy. Soc. Can*., Vol. 23, pp. 95-118, 1929.

Tiederman, W. G., Luchik, T. S., Bogard, D. G., "Wall-layer structure and drag reduction," *Journal of Fluid Mechanics*, Vol. 156, pp 419-437, 1985.

Toms, B., in *Proceedings of the International Congress of Rheology Amsterdam*, Vol. 2.0, pp. 135-141, 1948.

Virk, P. S., Merril E. W., Mickley, H. S., Smith, K. A., and Mollo-Christensen, E.L., "The Toms phenomenon—turbulent pipe flow of dilute polymer solutions," *Journal of Fluid Mechanics*, Vol. 30, pp. 305-328, 1967.

Walsh, M. J., "Drag characteristics of V-groove and transverse curvature riblets," In *Viscous Flow Drag Reduction* (ed G. R. Hough), *Progress in Astronautics and Aeronautics,* Vol. 72, pp. 168-184. 1980.

Walsh, M. J., "Turbulent boundary layer drag reduction using riblets," AIAA Paper 82-0169, 1982.

Walsh, M. J., "Riblets as a viscous drag reduction technique," *AIAA Journal*, Vol. 21, pp. 485-486, 1983.

Watanabe, O., Masuko, A., and Shirase, Y., "Measurements of drag reduction by microbubbles using very long ship models," *J. Soc. Naval Arch. Jpn*, Vol. 183, pp. 53-63, 1998.

White, C. M., Somandepalli, V. S. R., Mungal, M. G., "The turbulence structure of drag-reduced boundary layer flow," *Experiments in Fluids*, Vol. 36, pp 62-69, 2004.

Yarin, A.L., "On the mechanism of turbulent drag reduction in dilute polymer solutions: dynamics of vortex filaments," *J. Non-Newtonian Fluid Mech*., Vol. 69, pp. 137-153, 1997.

Vita

Kevin Chek-Shing Marr was born on January 6, 1982 in Dallas, Texas. He Graduated from Plano Senior High School in May 2000. In August of 2000 he enrolled in the University of Texas at Austin where he worked as an Undergraduate Research Assistant for 3 years. In December 2003, he graduated with a Bachelor of Science and in June 2004, he entered the graduate school in aerospace engineering at the University of Texas at Austin.

Permanent Address: 3324 Sandy Trail Ln
Plano, Texas 75023

This thesis was typed by the author